FACULTY OF SCIENCE AND TECHNOLOGY

BACHELOR'S THESIS

Study programme / specialisation: Mechanical Engineer	The spring semester, 2023 Open
Author: Mats Alsnes Sindre Slettemoen Haga	Mats Alsnes..... Sindre S Haga.....
Supervisor at UiS: Knut Erik Teigen Giljarhus	
Thesis title: Experimental testing of the new wind tunnel at the University of Stavanger	
Credits (ECTS): 20	
Keywords: Aerodynamics, Wind tunnel, Circular disk, Cylinder, Step Cylinder, Blockage correction.	Pages: 55 + appendix: 3 Stavanger, 15.05.2023

Acknowledgments

We express our gratitude to our supervisor, Dr. Knut Erik T. Giljarhus, for not only providing an excellent thesis topic but also for his great support and guidance throughout this project. The subject matter of our thesis was of great interest to both of us.

As this thesis marks the end of a three year bachelor program, we would also like to thank all professors and lab engineers who have been a part of our academic journey, as well as our families and close friends for the support during this time.

Summary

This thesis aims to gain experience in using the newly installed CTO S.A open circuit wind tunnel at the University of Stavanger. Extensive research has been done on the topics of wind tunnel use, general aerodynamics, blockage-correction methods, and other methods necessary to obtain accurate data. This thesis also presents the configuration and details of the specific wind tunnel used.

Wind tunnel tests have been performed on several geometries, these are circular flat disks, cylinder and step cylinder. Designing of geometries and modifications to the tunnel was done prior to the testing.

Blockage- correction methods and other methods has been applied to the results for comparison. Our results on the circular disk and cylinder is also compared to previous results from tests on the same geometries to ultimately gain insight and usability of all the methods.

The drag characteristics of the step cylinder is compared to the drag characteristics of uniform cylinders.

The corrected drag coefficients for the 200mm circular disks corresponds well to previous results. However, the corrected drag coefficients for the 50, 100, and 150mm disks deviates to a varying degree, due to unknown fault in the image method.

Comparing the corrected drag coefficients of the cylinder at different Reynolds numbers with previous results from "two-dimensional flow" experiments reveals clear similarities. However, the magnitude of the corrected drag coefficients appears to correspond better to the previous results obtained for cylinders with an aspect ratio of 5. When comparing flow separation angles on the cylinder using different techniques, inherent differences are observed, both for laminar and turbulent boundary layer.

The step cylinder drag coefficient is overall lower compared to drag coefficient of uniform cylinders, showing that calculating drag forces and drag coefficient can not be done accurately by only combining data on forces and coefficients from "two dimensional flow". The drag coefficient for a step cylinder will most likely be lower overall, where the extent of the difference depends on the diameter ratios.

Conclude on the most accurate blockage- correction method can not be done with our limited results where all seem effective. However it can be assumed that the Maskell III method is more accurate than Maskell's method since it also considers the wake distortion.

Contents

List of Figures

List of Tables

Nomenclature

Acronyms	Description	
CFD	Computational fluid dynamics	
FDM	Fused deposition modeling	
UiS	University of Stavanger	

Symbols	Description	Units
A	Area	m^2
A_f	Frontal area of body	m^2
A_s	Stream cross-sectional area	m^2
a	Accuracy	
C_D	Drag coefficient	
C_{Dc}	Corrected drag coefficient	
C_{DcM}	Corrected drag coefficient using Maskell's method	
C_{Dp}	Pressure drag coefficient	
ΔC_{DW}	Drag increment due to wake distortion	
C_p	Pressure coefficient	
C_{pb}	Base pressure coefficient	
C_{pbc}	Corrected base pressure coefficient	
c	Chord length	m
c_i	Sensibility coefficient	
D	Diameter	m
D_e	End- plate diameter	m
D_h	Hydraulic diameter	m
F_D	Drag force	N
F_{Df}	Friction drag force	N
F_{Dp}	Pressure drag force	N

Symbols	Description	Units
f_s	Shedding frequency	s^{-1}
h_b	Height of body	m
L	Length	m
P	Pressure	Pa
P_a	Atmospheric pressure	Pa
P_{sat}	Water vapor saturation pressure	Pa
P_{st}	Static pressure	Pa
P_{stag}	Stagnation pressure	Pa
P_v	Partial vapor pressure	Pa
P_∞	Free stream static pressure	Pa
q	Dynamic pressure	Pa
q_c	Corrected dynamic pressure	Pa
R_d	Gas constant of dry air	J kg^{-1} K^{-1}
Re	Reynolds number	
Re_x	Reynolds number in boundary layer	
RH	Relative humidity	%
r	Radius	m
St	Strouhal number	
s	Step size (numerical integration)	Radians
T	Temperature	Kelvin
t_C	Temperature	Celsius
u_i	Uncertainty contributions	
V	Fluid velocity	m s^{-1}
V_∞	Upstream velocity	m s^{-1}
w_b	Width of body	m
X_i	Quantity	
x	Distance (from leading edge)	m

Symbols	Description	Units
x_i	Estimate (measured value)	
δ	Boundary layer thickness	m
ε	Blockage factor	
θ	Angle	Radians
Λ	Shape factor	
μ	Dynamic viscosity	kg $m^{-1}s^{-1}$
ν	Kinematic viscosity	m^2s^{-1}
ρ	Density	kg m^{-3}
σ_i	Standard uncertainty	

1 Introduction

Aerodynamics can be described as the study on how air moves around objects and is an important aspect in a variety of different fields. All of which has one thing in common, a body is exposed to air flow. Whether the focus is on performance, stability or safety, wind tunnels are a useful tool to simulate these situations.

Carrying out tests in wind tunnels gives a better understanding of how the aerodynamics of an object is in real life, whether the object is an automobile, plane, boat, bridge, building etc. Testing can be done in full scale, or down-scaled to be more suitable for the wind tunnel available. The tests will output data to use directly or in further calculations and studies.

The University of Stavanger (UiS) have invested in a subsonic wind tunnel for educational and research purposes. The tunnel was ready to use in January of 2023. This bachelor thesis aims to gain experience and confidence in wind tunnel testing and to lay the foundation for further use of the facility. The tests conducted in this thesis will include collecting data on forces, surface pressures and flow visualizations. The results will be compared with previous studies and computational fluid dynamics (CFD) simulations.

1.1 Objective

This study will focus on testing circular flat disks of varying diameters (50, 100, 150, and 200 mm), a cylinder with surface pressure measuring capabilities and a step cylinder. Flat disks have been studied extensively, for instance in aerospace oriented studies such as stalled wings (e.g. E. C. Maskell [1]) Cylinders in the context of aerodynamics have also been studied a number of times due to its common appearance in designed structures (e.g. L. Prandtl [2])

A variety of methods used in wind tunnel testing will be described and where results from these is compared to previous results, hence why the disk and cylinder geometries was chosen due to its extensive data and results available. The purpose of these comparisons on methods is for further use of the wind tunnel.

While the geometry of a step cylinder is frequently observed in structures, it has not received nearly as much attention in research as the other geometries. A concrete example of a step cylinder geometry is the use of buoyancy elements attached to cables running from offshore wind turbines [3]. Studies on the drag characteristics by simulating the flow conditions that it will experience will be done and compared to uniform cylinders.

1.2 Limitations

The physical size of the test section and due to the maximum flow velocity of about $43\,\mathrm{m\,s^{-1}}$ limits the achievable Reynolds numbers, making it challenging to compare geometries with large size difference due to blocking effects.

Due to the open circuit design, the surroundings plays a role in the testing and output data. The outside wind can make it difficult to maintain the desired velocity and cause fluctuations in force and velocity measurements at lower velocities resulting in large uncertainties in the data received.

The flow velocity shown in the wind tunnel display seems to freeze/ lag at around $32\,\mathrm{m\,s^{-1}}$ to $35\,\mathrm{m\,s^{-1}}$. Testing in this region is done somewhat blindly.

2 Theory

2.1 Aerodynamics

Air surrounds the majority of man-made structures and we therefore are inevitably affected by it in some way. Aerodynamics is therefore an important aspect to consider when designing new structures.

The geometries in relation to aerodynamics can be divided into streamlined or bluff bodies. If a body is streamlined the fluid flow over it follows the contours of the body. An aerofoil is an example of a streamlined body. On the other hand a body is said to be bluff if the flow only partly (or not at all) follows the contours of the body. Example of a bluff bodies is cylinders. A disk can be considered both as bluff and streamlined depending on the orientation of the disc compared to he direction of the flow. It is considered as bluff if the direction of the flow is normal to the surface of the disk, and it is considered to be streamlined if the flow direction is parallel to the surface of the disk. [4].

2.1.1 Flow

In aerodynamics, the flow is divided into two categories; laminar and turbulent. There is also a transition region between the laminar and turbulent flow [5]. Usually there is a combination of laminar and turbulent flow over a body. To determine if the flow is laminar or turbulent Reynolds number is used. The Reynolds number is a dimensionless number defined by the ratio between the inertial forces and the viscous forces, and is given by

$$Re = \frac{\rho V D_h}{\mu} = \frac{V D_h}{\nu} \tag{2.1}$$

Where ρ is the fluid density, V is the uniform velocity of the fluid, D_h is the hydraulic diameter of the test object and μ is the dynamic viscosity of the fluid. ν is the kinematic viscosity of the fluid and is given by $\nu = \mu/\rho$ [5]. The hydraulic diameter used depends on the body being tested. If it is a cylinder the diameter is used, while for an aerofoil the chord length is used.

Boundary layer
When considering a body in aerodynamics, a fluid flow is passing a solid surface. Experimental results show that fluid in direct contact to the surface sticks to it and the fluid will not slip [6]. This is referred to as the no-slip condition. Due to this condition, the flow above it is also affected creating a gradually increase in velocity in the direction normal to the surface tangent. This region where the velocity is affected by the no-slip condition is referred to as the boundary layer [6]. An illustration can be seen in Figure 1.

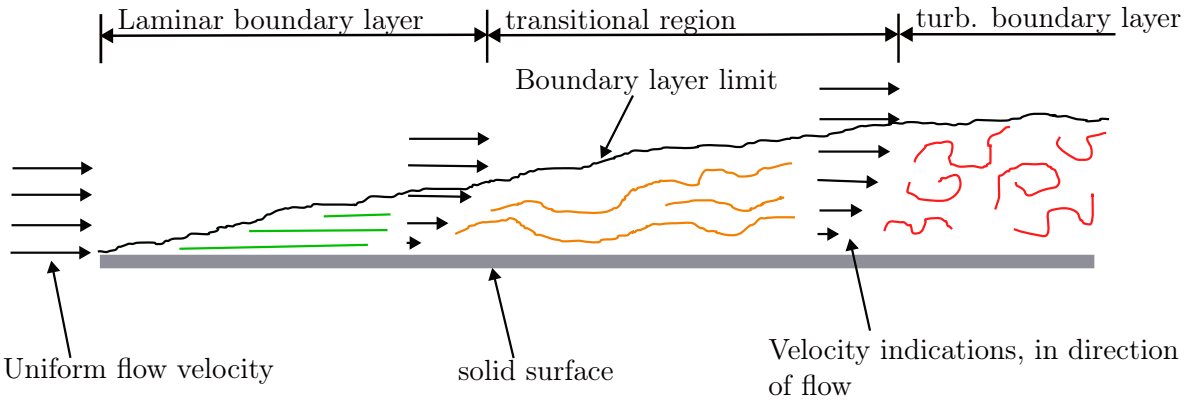

Figure 1: Illustration of the boundary layer development on a solid surface

The flow conditions within the boundary layer is first laminar at the leading edge of the plate before going into a transition- region and ending up as turbulent (see Figure 1). Where the transition between the types of flow conditions happens depends on the surface geometry, surface roughness, upstream velocity and more [6]. The variation in Reynolds number within the boundary layer along the surface is described by Equation (2.2):

$$Re_x = \frac{\rho V x}{\mu} \tag{2.2}$$

where V is the upstream velocity of the fluid and x is the distance from the leading edge of the solid surface [6].

Air density

For simplicity the air density is often calculated by the Ideal gas equation. This however does not take into account the relative humidity which changes the density of the air depending on the temperature and pressure. Air consists of nitrogen (78.08%), oxygen (20.95%), a small percent of other gases and a variable amount of water vapor. Humid air is less dense than dry air because a H_2O molecule (18 g/mol) weights less than oxygen (32 g/mol) and nitrogen (28 g/mol) [7]. Taking this into account the calculation of the air density becomes

$$\rho_{\text{humid air}} = \left(\frac{P}{R_d T}\right)\left(1 - \frac{0.378 P_v}{P}\right) \tag{2.3}$$

where P is the absolute pressure, R_d is the gas constant of dry air (=287.05 J/kg K), T is the temperature in Kelvin and P_v is the partial pressure of water vapor. The partial pressure of water vapor is calculated from

$$P_v = RH \times P_{sat} \tag{2.4}$$

where RH is the relative humidity, and P_{sat} is the saturation vapor pressure which is given by

$$P_{sat} = 610.78 \times 10^{\frac{7.5t_C}{t_C+237.3}} \tag{2.5}$$

t_C is the temperature in Celsius. [7]

Pressure coefficient
A dimensionless parameter, the pressure coefficient (C_p), is commonly used to describe the pressure distribution on a surface in fluid flow which can be used to calculate the drag force as explained in Section 2.7.1. It is defined as the difference between the total pressure at one point (P) on the surface and the free- stream static pressure(P_∞), divided by the dynamic pressure of the flow [6] giving:

$$C_p = \frac{P - P_\infty}{\frac{1}{2}\rho V^2} \tag{2.6}$$

2.1.2 Drag

The interaction between the flowing fluid and surface of the body submerged in the flow is often referred to as drag force (or simply just drag). The drag force direction is parallel to the air flow direction. Understanding drag is essential for engineers when designing automobiles, aircrafts, ships, windmills, towers, and other constructions exposed to fluid flow [8]. In the design of cars, aircrafts and ships it is desirable to reduce the drag to reduce fuel costs and obtain higher speed. When designing buildings it is important to ensure stability and thus safety.

To represent the drag characteristics of an object, a drag coefficient is used. The drag coefficient varies with fluid velocity, flow direction, geometry and size of object, fluid density and fluid viscosity [8]. It is given by

$$C_D = \frac{F_D}{\frac{1}{2}\rho V^2 A} \tag{2.7}$$

where A is frontal area and F_D is drag force. For a cylinder of finite length the frontal area is given by length times the diameter; $A = LD$. For airfoils and flat disks the area used is the area parallel to the flow, often called planform area, which is $A = cL$, where c is the chord length, for airfoils and $A = \frac{\pi D^2}{4}$ for a flat disk [8].

The drag coefficient can be divided into two parts; friction drag and pressure drag. Friction drag is caused by the wall shear stress while pressure drag is caused by the pressure distribution around the body [8]. For parallel flow over a flat disk the friction drag is most significant because of the large area on the top and bottom compared to the area in the front and back. On the other hand, for normal flow on a flat disk the pressure drag is most significant due to the large frontal area.

For a cylinder the friction drag is most significant at $Re \leq 10$ because the flow wraps around the cylinder (creeping flow). The pressure drag is most significant at $Re \geq 5000$ due to the flow separation at the back of the cylinder creating a low pressure wake behind it. At the intermediate Reynolds number both friction- and pressure drag are significant [8].

For an airfoil both friction- and pressure drag is significant. At low Reynolds number the drag is mostly due to friction drag as there is no flow separation. At higher Reynolds numbers separation at the rear of the body starts occurring creating a low pressure region. When the boundary layer goes from laminar to turbulent the friction drag increases resulting in an increase in the drag coefficient [8].

Friction- and pressure drag is hard to measure separately and it is usually most relevant to use the total drag coefficient. The total drag coefficient for common geometries at given Reynolds numbers can be found in tables and graphs. However in many cases the best solution is to measure the drag force for an object at different Reynolds numbers and calculate them from Equation (2.7) above [8]. The drag force can be measured in a wind tunnel at different wind velocities.

2.1.3 Wind tunnels

When designing a construction where the aerodynamic aspect is of importance, a way to simulate air flow past a body or geometry is needed. Wind tunnels have therefore been developed and designed to produce a uniform and steady air stream trough a test section. The body or geometry under consideration is placed in the test section to study the aerodynamics. The concept was first developed in the 1870s and has since been improved to yield more accurate results [9]. The development has resulted in many different configurations, but they are usually divided into two basic types. The first type is a closed circuit tunnel where the air is circulated in a closed system. The second type, is an open circuit tunnel which sucks air from the surroundings and exhausts it back into the surroundings [10].

The closed circuit type, due to the enclosed environment, has the ability to adjust the air quality to desired conditions. The downside of this, due to more complex design and more components, the closed circuit type is the more expensive to build and maintain [10]. In order to obtain numerical data from the body being tested, wind tunnel test sections are equipped with various devices. These devices include sensors that can measure forces, torque and pressures at specific locations on the body's surface. Additionally, upstream velocity measurement and temperature devices are also of significant importance.

Sometimes the objective is to visualise the flow around the the body. Methods commonly used for this is adding smoke to air stream, placing tufts on body surface or coating the surface with fluids of higher viscosity often referred to as flow- viz paint.

Computational simulations (CFD) is often carried out before the wind tunnel testing to

reduce costs from using the wind tunnel. The results are then compared to discover errors in the simulations and to improve further simulations.

2.1.4 Support interference

When conducting wind tunnel tests on models, there will always be one or more supports involved to fix the models position. These supports influences the fluid flow and leads to inaccurate test results if not properly taken into account. The magnitude of the influence depends on various factors such as the geometry of the model, the test section, the placement and the geometry of the support. Due to the significant variations in support interference from one setup to another, it is not feasible to develop a universal correction method. Instead, one have to analyze the influence from the support for each test setup. Some procedures for analyzing the support interference have been developed such as using the image method [10] or using computational fluid dynamics (CFD) to analyse the influence of the supports.

When using the image method in the case of a circular disk, first the original test setup is tested (see Figure 2a). The force measured from this is the force acting on the disk, the force acting on the support, the interference that the support has on the disk as well as the interference that the disk has on the support:

$$F_{\text{test 1}} = F_{\text{disk}} + F_{\text{support}} + I_{\text{support}} + I_{\text{disk}} \tag{2.8}$$

Secondly, a "dummy support" identical to the actual support is mounted in the tunnel test section, but not connected to the model and a new test is performed (see Figure 2b). By doing this the forces on the model and support is measured under the influence of the dummy support and the measured force is:

$$F_{\text{test 2}} = F_{\text{disk}} + F_{\text{support}} + I_{\text{support}} + I_{\text{dummy support}} + I_{\text{disk}} \tag{2.9}$$

Since the support and dummy support are practically identical, then $I_{\text{support}} = I_{\text{dummy support}}$. Finally the model is only attached to the dummy support (see Figure 2c) and the measured force is:

$$F_{\text{test 3}} = F_{\text{support}} + I_{\text{disk}} \tag{2.10}$$

By combining Equation (2.8), (2.9) and (2.10) and rearranging for F_{disk} gives: [10]

$$F_{\text{disk}} = 2F_{\text{test 1}} - F_{\text{test 3}} - F_{\text{test 2}} \tag{2.11}$$

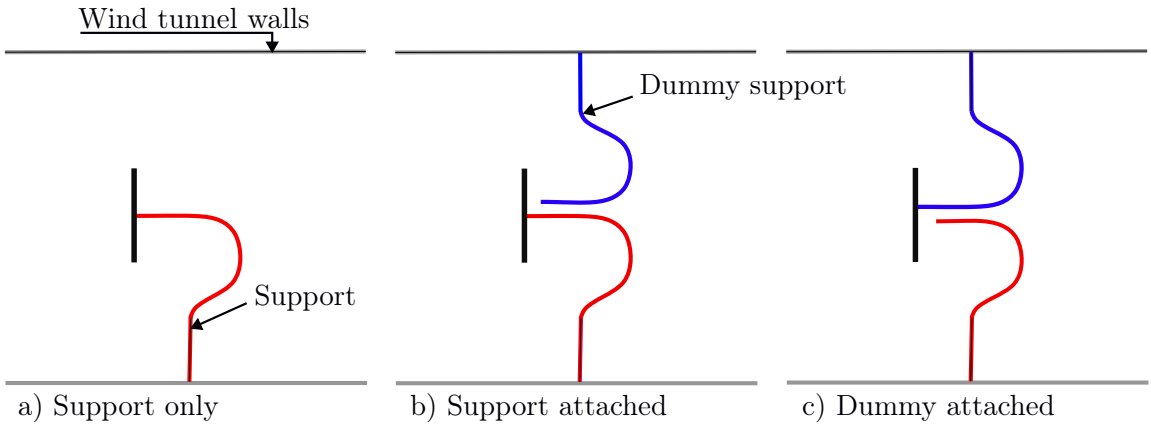

Figure 2: Analyzing support interference by dummy support

2.2 Correction methods

It's important to note that there are inherent differences in flow conditions when testing in a wind tunnel versus open air. In the case of this study, the test section is a closed test section, meaning that the location where test bodies are placed is enclosed and isolated from the surroundings. Due to this enclosed environment, the air flowing around the test body is somewhat restricted, leading to deviations in measurements compared to values that one would achieve in an unlimited stream. The extent of these deviations depends on the ratio between frontal area of the body and cross-sectional area of the wind tunnel test section (the stream cross-sectional area), called the blockage ratio. Typically, this ratio is chosen to be in the range $0.01 \leq \frac{\text{frontal area}}{\text{stream area}} \leq 0.1$ [10]. Higher ratios could lead to more inaccurate results.

Correction methods have been developed to account for these deviations. The relevant correction methods for the bodies considered in this report are discussed below.

2.2.1 Horizontal buoyancy corrections

The walls of a test section generate boundary layers with increasing thickness along the length of the section. This results in a static pressure drop along this length and with the pressure drop, an increase in velocity [10]. The pressure drop produces an additional drag force due to the difference in static pressure over the length of the body being tested. For the geometries tested in this report, due to their short length in the flow direction, the additional drag force is neglected. The velocity increase from the start of the test section to where objects are placed is discussed more in Section 2.7.

2.2.2 Blockage corrections

Maskell's method

E. C. Maskell's work [1] describe a blockage correction method for bluff bodies based on momentum balance (conservation of momentum) in the flow. Considering only the effects associated with flow separation. His theory provides an estimate of the ratio between corrected dynamic pressure and measured dynamic pressure given in Equation (2.12). It is important to notice that the following equations are neglecting induced drag and profile drag.

$$\frac{q_c}{q} = \frac{1 - C_{pb}}{1 - C_{pbc}} = 1 - \frac{C_D}{C_{pbc}} \cdot \frac{A_f}{A_s} \tag{2.12}$$

Where q is dynamic pressure (measured), q_c is corrected dynamic pressure, A_f is frontal area of body, A_s is the cross-sectional area of the air-stream, C_{pb} is the base pressure coefficient and C_{pbc} is the corrected base pressure coefficient.

The corrected base pressure coefficient have been previously computed for a circular disk by Fail, Lawford and Eyre in their work [11], to be -0.36. Maskell also studied if wall constraints can be regarded as equivalent to a increase in the unlimited fluid velocity [1]. His experiments supported this theory to some degree of accuracy and from this came the relation of ratio for drag coefficients and dynamic pressures in:

$$\frac{q_c}{q} = \frac{C_D}{C_{Dc}} \tag{2.13}$$

C_{Dc} is corrected drag coefficient. For more information about Maskell's theory, experiments and this relation see [1].

Equation (2.12) is commonly rewritten as (for bluff body use):

$$\frac{q_c}{q} = 1 + \varepsilon C_D \frac{A_f}{A_s} \tag{2.14}$$

where Maskell suggests the blockage factor $\varepsilon = \frac{5}{2}$ as a satisfactory approximation for three dimensional flow[1].

Rearranging Equation (2.13) and (2.14) for the corrected drag coefficient gives:

$$C_{Dc} = \frac{C_D}{1 + \varepsilon C_D \frac{A_f}{A_s}} \tag{2.15}$$

Maskell III method

An extension to Maskell's method is developed by J. E. Hackett and K. R. Cooper [12], named Maskell III. This method, in addition to flow separation, accounts for the wake distortion induced by the body. Before conducting the dynamic pressure correction (as in

Maskell's method), this method removes the drag increment due to the wake distortion, ΔC_{DW} and is later added in the calculation of final correction. Corrected drag coefficient using Maskell's method is in further equations named C_{DcM} to distinguish from from the final corrected drag coefficient.

Subtracting ΔC_{DW} from C_{DcM} in (2.15) and with further rearranging gives [12]:

$$C_{DcM} - \Delta C_{DW} = \frac{-1 + \sqrt{1 + 4\varepsilon C_D \frac{A_f}{A_s}}}{2\varepsilon \frac{A_f}{A_s}} \tag{2.16}$$

Values for ε from Maskell's results [1] has been fitted to an equation [13]:

$$\varepsilon = 0.96 + 1.94e^{-0.12\frac{h_b}{w_b}} \tag{2.17}$$

h_b is height of body and w_b is width of body.

The increment due to drag distortion is given by [12]:

$$\Delta C_{DW} = C_D \left[\frac{1}{1+x} + \frac{1 - \sqrt{1+4x}}{2x} \right], x = \varepsilon C_D \left(\frac{A_f}{A_s} \right) \tag{2.18}$$

The dynamic pressure correction is expressed as:

$$\frac{q_c}{q} = 1 + \varepsilon C_D \frac{A_f}{A_s} - \Delta C_{DW} \tag{2.19}$$

Finally, the total correction is given by:

$$C_{Dc} = \frac{C_D}{1 + \varepsilon \frac{A_f}{A_s} \left(C_{DcM} - \Delta C_{DW} \right)} + \Delta C_{DW} \tag{2.20}$$

Awbi's correction method

The correction method H.B. Awbi came up with in his phd. thesis [14] is well described in [15]. His method is also a modification to Maskell's method using Equation (2.14). Awbi's method includes a term known as the shape factor. It was included for use on bluff bodies with different geometry than the flat square plate used in Maskell's experiments. Equation (2.14) becomes:

$$\frac{q_c}{q} = 1 + \Lambda \varepsilon C_D \frac{A_f}{A_s} \tag{2.21}$$

where $\varepsilon = 5/2$ and Λ is the shape factor given as:

$$\Lambda = \left\{ \begin{array}{ll} 1.11 + 0.94\frac{w_b}{h_b} & \text{for } 0 < \frac{w_b}{h_b} \leq 0.5 \\ \\ 1.11 - 0.14\frac{w_b}{h_b} & \text{for } 1 < \frac{w_b}{h_b} \leq 5 \end{array} \right\} \tag{2.22}$$

The equation for the corrected drag coefficient is then:

$$C_{Dc} = \frac{C_D}{1 + \Lambda \varepsilon C_D \frac{A_f}{A_s}} \tag{2.23}$$

2.3 Circular disk

Circular disks and flat plates have been studied extensively in the context of aerodynamics, particularly in aerospace-oriented studies such as stalled wings e.g. E. C. Maskell [1]. The drag coefficient of disks is practically constant as the Reynolds number increases above 1000, and this behavior persists even at the highest Reynolds number ever measured, which is close to 10^7 [16]. Drag coefficients in this region (Re >1000) from different studies testing circular disks, is shown in Table 2 for comparison.

Table 2: Summary of results and test info. from studies on circular disks

Re	C_D	Blockage- ratio (%)	Contributors
3.4×10^4	1.13*	0.97	D. J. Craze [17]
1.7×10^5	1.15*	1.36	D. J. Craze [17]
2.09×10^5	1.12*	1.45	Fail, Lawford and Eyre [11]
5 - 10^5	1.17	1.23	F. W. Roos and W. W. Willmarth [18]
3.3×10^4 - 2.28×10^5	1.15	0.4	M. Knight [19]
6.5×10^4 - 4.55×10^5	1.18	1.78	M. Knight [19]
9.8×10^4 - 6.82×10^5	1.31	4.00	M. Knight [19]
2.1×10^5 - 4.44×10^6	1.11	0.97	J. M. Shoemaker [20]
3.62×10^3 - 9.62×10^5	1.11	open	L. Prandtl [2]

Drag coefficients marked with (*) have been blockage corrected.
M. Nights, L. Prandtl, J.M Shoemaker, F. W. Roos and W. W. Willmarth's listed C_D in Table 2 is their averaged result from tests with varying Reynolds numbers, rounded to two decimals, for easy comparison only. All tests were performed in wind tunnels except for the tests conducted by F. W. Roos and W. W. Willmarth, which were performed in a glycerine/water-filled channel. L. prandtl's tests were performed in a open test section.

From these results it is clear that different tests gives some variations in the drag coefficient. One explanation for this is variations in degree of turbulence in the fluid stream [16]. Another explanation is the blocking effect that will occur in wind tunnels and the use of correction methods [16].

2.4 Cylinder

Fluid flow over a cylinder is a common phenomenon, such as fluid flowing over a pipeline in the sea, circular trusses on a bridge, or windmill towers. Cylinders have been studied extensively and a large amount of data from previous experiments are available. For data on drag coefficients vs. Reynolds number, the studies of L. Prandtl [2] and C. Wieselsberger [21] are used for comparison in this report. C. Wieselsberger's studies where all taken in "uniplanar flow" meaning the flow is "two dimensional" as in Figure 3. L. Prandtl's study include both a test of an "infinitely long cylinder", also meaning the flow is "two dimensional" and a test of a cylinder with a length over diameter ratio (aspect ratio) of 5.

In the case of a cylinder, the diameter, D, is used in Equation (2.1) to calculate the Reynolds number. The critical Reynolds number for flow across a circular cylinder is $Re_{cr} \approx 2 \times 10^5$. The boundary layer is laminar up to about $Re \leq 2 \times 10^5$, transitional for $2 \times 10^5 \leq Re \leq 2 \times 10^6$ and turbulent for $Re \geq 2 \times 10^6$ [8], where surface roughness can contribute to transitional and turbulent boundary layer at lower Reynolds numbers [22].

Flow over a cylinder leads to complex flow patterns. As the fluid approaches the cylinder, it follows the curvature of the cylinder before separating at a point at the top or slightly towards the back of the cylinder [8]. This forms a separation region in the back of the cylinder with a turbulent behaviour and low pressure referred to as turbulent wake in Figure 3. At one point in the middle of the front of the cylinder the fluid particles hits the surface at the stagnation point and raising the pressure at this point. The difference in the pressure in the front and the back of the cylinder leads to a pressure drag.

When $Re \leq 1$, the flow is "creeping". Then the fluid flow is not separating and flows along the surface all the way around the cylinder. In this case the pressure is the same on both sides resulting in no pressure drag, only friction drag [8].

Where the separation occurs depends if the flow is laminar or turbulent. When the flow is laminar the separation occurs at $\theta \approx 80°$, while the separation occurs at $\theta \approx 140°$ when the flow is turbulent (see Figure 3). The delayed separation at turbulent flow is due to the rapid fluctuations of the fluid along the surface, enabling the turbulent boundary layer to remain attached to the surface longer. This results in a narrower wake which leads to lower pressure drag [8].

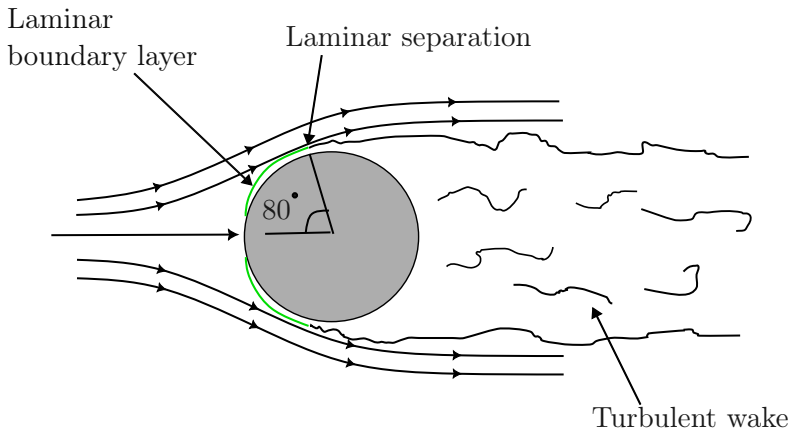

a) $\text{Re} \leq 2 \times 10^5$

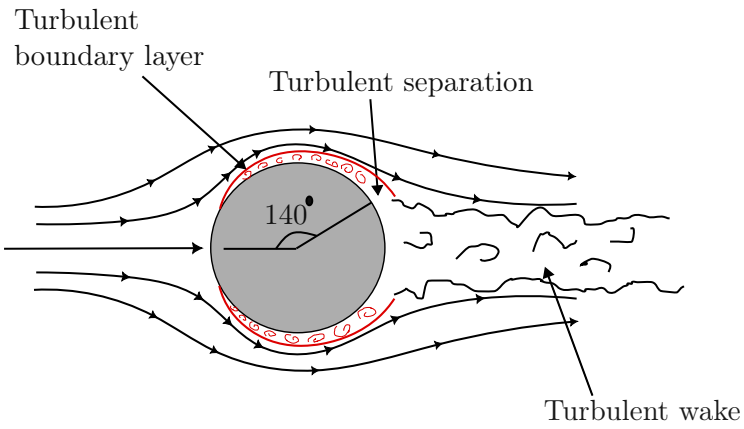

b) $\text{Re} \geq 2 \times 10^6$

Figure 3: Illustration of 2D flow past a cylinder with: a) laminar boundary layer and b) turbulent boundary layer

2.4.1 Drag crisis

The drag coefficient on a cylindrical body is affected by where the separation occurs. As the Reynolds number increases, the separation point moves forward until reaching $\theta \cong 90°$. At this point the drag coefficient seems to converge, but as the Reynolds number reaches $10^5 - 10^6$ (depending on the surface roughness) the boundary layer becomes turbulent. In the transition of the boundary layer from laminar to turbulent the separation point is delayed to $\theta \cong 140°$, resulting in a narrower wake (see Figure 3b). When the the wake is

closing the pressure drag decreases rapidly and thus the drag coefficient decreases. This phenomenon is referred to as the drag crisis [8].

2.4.2 Interference on cylinders

For cylinders with large aspect ratios such as steel wires or cables, the flow is taken to be "two dimensional" [23] as in Figure 3. To achieve this essentially two dimensional flow past a cylinder in a wind tunnel is proven to be a difficult task. The interference of the surface boundary layer that the cylinder is fixed to and the flow over the free end(s) results in a more complex three dimensional flow [24]. The flow past a free end can create a higher pressure (base pressure) on the backside compared to a two dimensional flow [25].
A common solution for the free end is the use of end- plates to isolate the flow around the cylinder. To be able to isolate the flow as best as possible and not introduce other significant interference, the geometry of the end- plate is of importance. Stansby, in his article [25] suggests a square plate with distance from cylinder axis to the leading edge to be 2.5 times the cylinder diameter, and the distance from the trailing edge to cylinder axis should be 4.5 times the diameter [26]. Fox and West, after their study [26] concluded with; if end-plates of these dimensions where to be used, the aspect ratio must be larger than a critical minimum of 7 to ensure a region with uniform base pressure and "two- dimensional" flow. After a series of tests on circular end plate sizes in [27], a more uniform base pressure and therefore more uniform drag coefficient was maintained along the length of the cylinder with end- plate diameter $D_e \geq 4d$, where d is cylinder diameter.

An important note from Stansby [25] is, even with uniform base pressure over most of the cylinder span, the flow may be far from two- dimensional [23].

2.4.3 Vortex shedding

Vortex shedding is a phenomenon in fluid dynamics where the fluid flowing over a bluff body causes the object to vibrate at a low frequency. As the fluid flowing over a body starts to separate from the surface it forms swirls which continues to spin as the fluid moves further away from the body. When a vortex forms along the surface of the body it creates a suction force. When there are enough vortices the suction becomes stronger resulting in a net force pulling the body over to that side. As the vortices are occurring on both sides of the body with varying velocities the forces creates a oscillating force causing the body to vibrate [28]. The frequency of the vibration (shedding frequency) can be found from

$$f_s = \frac{StV_\infty}{L} \tag{2.24}$$

where St is the Strouhal number, V_∞ is the upstream velocity and L is the characteristic length of the body (diameter in the case of a cylinder). The Strouhal number depends on

the cross sectional shape of the body and is a function of Reynolds number. In the range $250 < \mathrm{Re} < 2 \times 10^5$ the Strouhal number can be calculated from the empirical formula [29].

$$St = 0.198(1 - \frac{19.7}{Re}) \tag{2.25}$$

Vortex shedding is important in designing of buildings, bridges and other slim objects. The pipelines in the sea and the piping inside a heat exchanger is affected by vortex shedding. If the shedding frequency equals (or almost equals) the natural frequency of the construction resonance can occur, potentially leading to failure [28].

2.5 Step cylinder

A step cylinder is a cylinder with a sudden reduction in diameter. The flow characteristics past a step cylinder is of interest due to its presence in many applications exposed to fluid flow. The geometry of a step cylinder is frequently observed in structures, but it has not received nearly as much attention in research as the other geometries. The main focus have been done on the flow characteristics and wake flow at low Reynolds numbers e.g. N. W. M. Ko and A. S. K. Chan [30], T. Cai et al. [31]. An example of a step cylinder geometry is the buoyancy elements attached to the cables running from offshore wind turbines [3]. Usually the currents in the North Sea varies from 0 to $1.6\,\mathrm{m\,s^{-1}}$, and can reach $2\,\mathrm{m\,s^{-1}}$ in some areas [3]. The diameter ratio D/d for the step cylinder is also a important factor where different ratios can yield different results. To study the effects of the current on the cable with buoyancy elements one can use a wind tunnel by scaling the velocity and model size.

The interest in this report will be comparing drag forces and coefficients of uniform cylinders versus step cylinder at higher Reynolds numbers.

2.6 CTO-LSWT-O-C1-0.2/40/1/22 wind tunnel

Following is technical information of importance about the wind tunnel used for tests/ studies in this report.

The CTO-LSWT-O-C1-0.2/40/1/22 Wind tunnel is (as the name implies) a low speed wind tunnel, open type, closed test section with 0.2 m^2 cross-sectional area , rated/capable of $40\,\mathrm{m\,s^{-1}}$ wind stream, 22kW motor [32].

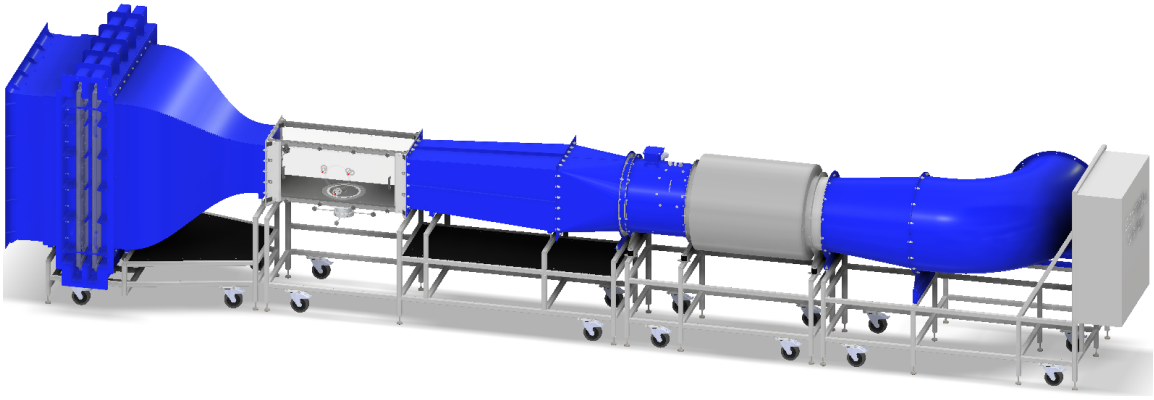

Figure 4: 3D model of wind tunnel used

Technical:

- Company/ brand: CTO S.A.
- Type: Open circuit
- Test section: Closed test section, measuring $450 \times 450 \times 1250$mm (Parallel walls)
- Velocity range (test section): 0- $40\,\mathrm{m\,s^{-1}}$
- Motor power: 22KW

Features:

- Rotary table Ø360mm (manual)
- Force and torque measurement in table in X,Y,Z axes, max. 80N/8Nm
- Velocity measurement using pitot tube
- Velocity measurement using pressure difference in inlet contraction
- Surface pressure measurements (max. 24 measuring points)
- Flow temperature measurement
- Smoke generator system (separate)

2.6.1 Components

The wind tunnel configuration and named components is shown in Figure 5.

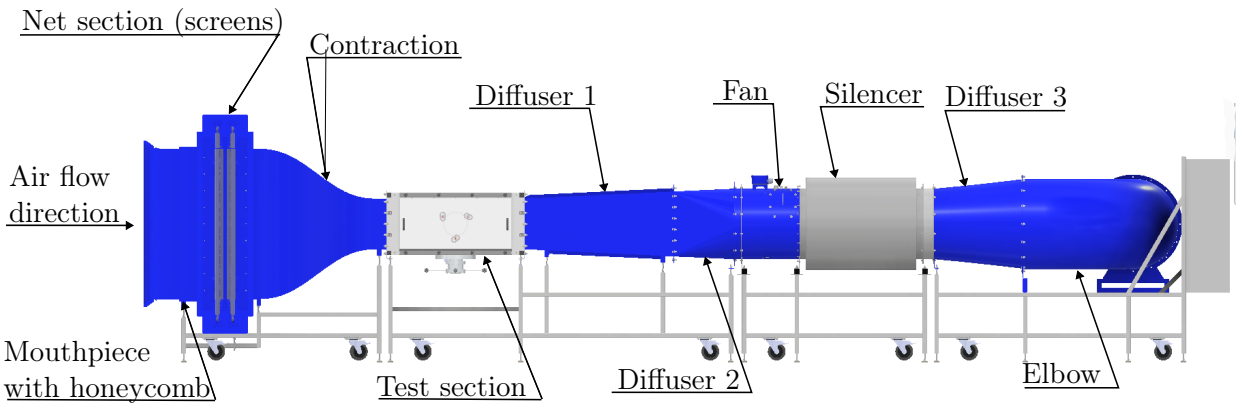

Figure 5: Presentation of the wind tunnel components

Mouthpiece with honeycomb
The first components the air passes trough is the Mouth piece and honeycomb. This ensures uniform suction of air and where the honeycomb forces the flow to go in the same direction [10] reducing turbulence in the lateral plane. The honeycomb cells are circular with 7mm diameter and 160mm deep [32].

Net section (screens)
In this particular tunnel the net section consist of two screens with square cells. The first screen has cell size of 1.25×1.25mm with wire thickness of 0.4mm. The second screen is a finer one with cell size of 0.56×0.56mm and wire thickness of 0.17mm [32]. The screens brings the various parts of the flow to a constant speed, reducing the axial turbulence. The more screens the more is the flow improved, but at the expense of lower pressures after the screens due to its blocking effects [33].

Contraction
By reducing the cross sectional area of the flow, the contraction increases the velocity of the air steam as well as improving uniformity in flow. The contraction is fitted with static pressure measuring points at the largest cross- sectional area and at the smallest. A Aplisens APR-2000G differential pressure sensor (range: -2500 to +2500 pa, accuracy: 0.25% of range [32]) measures the differential pressure between the two points. This is to calculate the flow velocity (further described in Section 2.7). The contractions shape is specially designed with smooth curvatures to not create air separation.

Test section
From the contraction, the flow continues trough the test section where bodies under con-

sideration is placed. The flow here is stated to have turbulence intensity $< 1\%$ [32]. The test section size is 450x450x1200mm and is equipped with pitot tube, rotary table and the possibility for surface pressure measurement. Placed in the rotary table is a CL16-3F/3M, Six-parameter force and torque sensor, able to measure force from 0 to 80N and moment from 0 to 8Nm in X, Y, Z axis. The pitot tube is used to measure flow velocity, with the use of an Aplisens APR-2000G differential pressure sensor (range: -700 to +700pa accuracy: 0.25% of range [32]). The calculation of flow velocity by using the pitot tube, is further described in Section 2.7.
Due to the smaller pressure range on the sensor for the pitot tube, it is more accurate but will be maxed out at $V \approx 33\,\mathrm{m\,s^{-1}}$. The pitot tube is then usually used from 0- $33\,\mathrm{m\,s^{-1}}$, then the velocity calculation is switched automatically to using the contraction.

To measure surface pressure, a SVM tec PSC24 differential pressure scanner is available. The scanner is capable of measure 24 simultaneous pressure signals in addition to one reference signal. The scanner has and an accuracy of +/- 0.25% between lowest and highest measured point (FSS) and the range is ±1250Pa [32].

Diffusers
The first diffusers role is to lower the flow velocity and increase static pressure, resulting in a efficiency increase. For this the diffuser has a slight increase in cross- sectional area over its length. The air temperature sensor (Aplisens CT-E1 Pt-100) is placed at the very beginning of the first diffuser (accuracy of pt-100 elements: ±0.1°C [34]).
Diffuser 2 has the purpose of making the transition form square cross- section to circular cross- section smoothly before entering the fan.
The diffuser 3 decreases the flow velocity further before the air is exited through the elbow.

Fan and silencer
Moving air trough the tunnel is done by a Planetfan KM 630/22,0-2/6/P7 fan. 6 blade, 630mm rotor diameter with a 22kW electric motor. From the fan, air passes trough a Planetfan TA630/1000 silencer with a suppression rating of 7dB (A) [32].

Smoke generator
A Ate Aerotech smoke generator is available with a hand held probe to visualize airflow.

2.7 Mathematical methods

2.7.1 Force by pressure

For bodies being tested, the force values in x, y and z direction given by tunnel instruments can be used, or it can be calculated from measuring surface pressure around the body and use this to calculate the forces. For a cylinder the drag force in the direction of flow can be calculated using pressure on the surface around the circumference of the cylinder, as

following equations describe.

The total drag force is given as:

$$F_D = F_{Dp} + F_{Df} \tag{2.26}$$

where F_{Dp} is pressure drag and F_{Df} is friction drag. As discussed, the total pressure will be highest at the stagnation point where the velocity is practically zero, and gradually lower moving towards the backside of the cylinder. Resulting in a integral along the circumference to obtain the pressure drag force in the direction of flow. A cross- section of the cylinder and an element of the integral is shown in Figure 6:

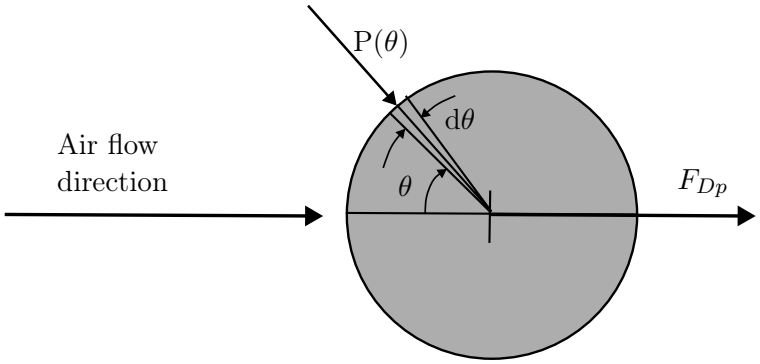

Figure 6: Cross-section of cylinder, illustrating an element of the integral for pressure drag.

The integral for the cylinder is a function of pressure at a specific angle and its force contribution in direction of flow [35]:

$$F_{Dp} = \int_0^{2\pi} (P(\theta) - P_{st}) r h_b \cos\theta \, d\theta \tag{2.27}$$

P_{st} is static pressure in free stream, r is cylinder radius, h_b is the cylinder height and θ is angle in radians. Assuming symmetric flow on both sides of the cylinder, one only needs to consider one side and multiply the result by two. With this, and taking out the constants radius and height, gives:

$$F_{Dp} = 2 r h_b \int_0^{\pi} (P(\theta) - P_{st}) \cos\theta \, d\theta \tag{2.28}$$

Further calculating the Pressure drag coefficient (C_{Dp}) with Equation (2.7) and Equation (2.28) gives:

$$\frac{F_{Dp}}{\frac{1}{2}\rho V^2 A} = \frac{2 r h_b \int_0^{\pi} (P(\theta) - P_{st}) \cos\theta \, d\theta}{\frac{1}{2}\rho V^2 A} \tag{2.29}$$

By recognizing that the frontal area cancels out, the right side of the equation is just Equation (2.6) times the cosine and finally we have Equation (2.30) for calculating the drag coefficient using the pressure distribution on the body surface [35]:

$$C_{Dp} = \int_0^{\pi} C_p \cos\theta \, d\theta \tag{2.30}$$

To measure the pressure on all points of the surface area on the other hand is close to impossible. Equation (2.28) or (2.30) must instead be solved numerically with a discrete set of data-points measured at the surface with a pressure scanner. Solving the integral with the Simpson 1/3 method (2.31) will give an acceptable approximation of the drag force value.

$$\int_a^b f(x)\, dx \approx \frac{s}{3}[f(x_0) + 4 \sum_{i=1,3,5,..}^{n-1} f(x_i) + 2 \sum_{i=2,4,6,..}^{n-1} f(x_i) + f(x_n)] \tag{2.31}$$

Where s is the step size between measuring points and n is number of measuring points. In the cylinder case $s = \frac{\pi}{n-1}$.

The friction drag accounts for about 50% of the total drag at $Re \leq 2$, but only about 7% with $Re = 1000$ [36]. For higher Reynolds number the friction drag is usually neglected and Equation (2.26) can be rewritten as $F_D \approx F_{Dp}$ and Equation 2.30 as $C_D \approx C_{Dp}$

2.7.2 Velocity

The wind tunnel used in this report includes two different ways of measuring flow velocity in the test section.

Contraction
The wind tunnel contraction is as described in Section 2.6, fitted with two static pressure measuring points and a differential pressure sensor measuring the pressure difference between the inlet (largest area) and outlet (smallest area) of the contraction.
With this pressure difference, Bernoulli equation (2.32) and the continuity equation in steady flow (2.33), calculations to determine velocity at the smallest area (at the start of test section) is done according to K. Nawacaki [37] as following:

$$P_1 + \frac{1}{2}\rho_1 V_1^2 + \rho_1 g h_1 = P_2 + \frac{1}{2}\rho_2 V_2^2 + \rho_2 g h_2 \tag{2.32}$$

$$\rho_1 A_1 V_1 = \rho_2 A_2 V_2 \tag{2.33}$$

Where the number 1 and 2 denotes the point at the largest cross- sectional area and at smallest cross- sectional area respectively. The contraction ratio A_1/A_2 on this particular contraction is 9 [32]. Density is assumed constant trough the contraction and is calculated with the use of the ideal gas equation rearranged for density [37]:

$$\rho_1 = \rho_2 = \frac{P_a}{R_d T} \tag{2.34}$$

Where T is Temperature in kelvin and P_a is atmospheric pressure measured by a (Aplicens PC-28/TR/80÷120kPa, uncertainty: 0.2% [32]) sensor located in close proximity to the wind tunnel.

Combining Equation (2.32), (2.33), (2.34) and rearranging for V_2 gives:

$$V_2 = \sqrt{\frac{2(P_1 - P_2)R_d T}{P_a[1 - (\frac{A_2}{A_1})^2]}} = \sqrt{\frac{2\Delta P(t_C + 273.15)R_d}{P_a[1 - (\frac{A_2}{A_1})^2]}} \tag{2.35}$$

A temperature correction is needed, as seen in the last expression in Equation (2.35) since the sensor in the air flow gives temperature values in Celsius (t_C). For the propagated uncertainty of the calculated velocity, see Section 2.7.3.

Pitot tube
The second method of measuring flow velocity is by using a pitot tube. The pitot tube has a measuring- point facing the flow measuring stagnation pressure, as well as static pressure measuring- points normal to the air stream. With the use of the difference in stagnation pressure at the tip of tube and the static pressure in the airflow entering the test section, as well as the Bernoulli's equation (2.32) and the Equation (2.34) for density, calculating flow velocity is done according to K. Nawacaki [37] as following:

$$V = \sqrt{\frac{2(P_{stag} - P_{st})}{\rho}} = \sqrt{\frac{2\Delta P(t_C + 273.15)R_d}{P_a}} \tag{2.36}$$

For the propagated uncertainty of the calculated velocity, see Section 2.7.3.

2.7.3 Uncertainty in calculated velocity

The velocity, as seen in Equation (2.35) and (2.36) depends on the measured differential pressure, temperature and atmospheric pressure. Each of these measuring devices have an accuracy listed. The total propagated uncertainty for the calculated velocity using the pitot tube and contraction can be calculated using the "Guide to the Expression of uncertainty in measurement" often referred to as GUM- method/ guide described in [38]. The accuracy for each sensor (referred to as quantity) in percentage and resulting values in units is listed in Table 3.

Table 3: Accuracy for sensors used for velocity calculations, in percentage and units.

Sensor	accuracy(±)(%)	accuracy in units (±)
Diff. pres., contraction	0.25	12.5pa
Diff. pres., pitot- tube	0.25	3.5pa
Atm. pressure	0.2	80pa
Temp.	-	0.1°C

There is two types of methods in the GUM- guide, type A and type B. Type A is described in the paper [38] as: "applied when several independent observations have been made for one of the input quantities under the same conditions of measurement". Type B is not based on the use of a series of data but rather data provided in calibration or manufacture specifications etc. For this type of data the type B evaluation of measurement uncertainty is then chosen. Considering the type of probability distribution, the paper [38] states: "If only upper and lower limits a+ and a– can be estimated for the value of the quantity Xi (e.g., manufacturer's specifications of a measuring instrument, a temperature range, a rounding or truncation error resulting from automated data reduction), a probability distribution with constant probability density between these limits (rectangular probability distribution) has to be assumed for the possible variability of the input quantity X_i.". The assumed rectangular probability distribution results in a standard uncertainty $\sigma_i = \frac{a_i}{\sqrt{3}}$. where a_i is the listed accuracy.

The sensitivity coefficient (c_i) for each quantity is the partial derivative of the velocity equation (2.35) with respect to the quantity (X_i) evaluated at the input values of each sensor (x_i) as Equation (2.37) implies:

$$c_i = \frac{\partial V}{\partial x_i} \tag{2.37}$$

To retrieve each contribution (u_i), the standard uncertainty is multiplied by the sensitivity coefficient. All information can then be organised as in Table 4:

Table 4: Arrangement of the quantities, estimates, standard uncertainties, type of probability distribution, sensitivity coefficients and uncertainty contributions, for $V = 43.4944\,\mathrm{m\,s^{-1}}$.

Quantity(X_i)	Estimate(x_i)	St. unc(σ_i)	Prob. distrub.	Sens. coef.(c_i)	unc. contrib.(u_i)
ΔP	1171.17pa	7.22pa	Rectangular	0.0187	$0.135\,\mathrm{m\,s^{-1}}$
P_a	102880pa	46.19pa	Rectangular	-2.1270×10^{-4}	$-9.836 \times 10^{-3}\mathrm{m\,s^{-1}}$
T_c	16.30 °C	0.058	Rectangular	0.0756	$4.362 \times 10^{-3}\mathrm{m\,s^{-1}}$
V	$43.4944\,\mathrm{m\,s^{-1}}$	-	-	-	$0.1491\,\mathrm{m\,s^{-1}}$

The sum of the uncertainty contributions are calculated as $u = \sqrt{u_1^2 + u_2^2 + u_3^2}$ [38]. Assuming a normal distribution of the output (calculated) velocity, and that the standard uncertainty for the output velocity has sufficient reliability, it is recommended in the paper [38] to use a coverage factor to expand the uncertainty by a factor $k = 2$ resulting in a coverage probability of approximately 95% [38]. This gives a total uncertainty of $0.2981\,\mathrm{m\,s^{-1}}$ and $V = 43.4944 \pm 0.298\,\mathrm{m\,s^{-1}}$.

Using this method for each velocity gives a list (Table 5) of all velocities and corresponding propagated uncertainty:

Table 5: Uncertainty for each calculated velocity

Method	Vel. ($m\,s^{-1}$)	uncertainty ($\pm\, m\,s^{-1}$)	Method	Vel. ($m\,s^{-1}$)	uncertainty ($\pm\, m\,s^{-1}$)
pitot	1.0969	2.988	pitot	23.0040	0.1570
pitot	1.9928	1.6449	pitot	24.0075	0.1516
pitot	3.0006	1.0929	pitot	25.0042	0.1468
pitot	4.0014	0.8203	pitot	26.0090	0.1423
pitot	5.0071	0.6565	pitot	27.0053	0.1384
pitot	6.0490	0.5439	pitot	27.9948	0.1347
pitot	7.0020	0.4709	pitot	29.0025	0.1316
pitot	8.0018	0.4136	pitot	30.0013	0.1286
pitot	9.0170	0.3680	pitot	31.0043	0.1257
pitot	10.0090	0.3333	pitot	31.9974	0.1228
pitot	11.0018	0.3045	pitot	32.9461	0.1207
pitot	12.0033	0.2802	Contraction	34.0148	0.3672
pitot	13.0036	0.2602	Contraction	35.0015	0.3584
pitot	14.0005	0.2428	Contraction	35.9925	0.3496
pitot	15.0024	0.2276	Contraction	37.0295	0.3413
pitot	16.0144	0.2145	Contraction	38.0041	0.3338
pitot	17.0090	0.2031	Contraction	39.0159	0.3268
pitot	18.0055	0.1929	Contraction	40.0011	0.3196
pitot	19.0095	0.1842	Contraction	41.0010	0.3130
pitot	20.0007	0.1764	Contraction	42.0046	0.3070
pitot	21.0017	0.1696	Contraction	43.1895	0.2999
pitot	22.0036	0.1631	Contraction	43.4944	0.2998

The velocity is further used in calculating Reynolds number, drag coefficients, Pressure coefficients etc. resulting in further error propagation with more uncertainties added. For instance; calculating drag coefficients using Equation 2.7, the uncertainties in the velocity, measured diameter (used to calculate area), calculated density and measured force should all be considered to determine the total uncertainty of the calculated drag coefficient, using the GUM-method for instance. However, this is not done for the results in this report due to the complexity and its time consume, but is added and discussed for the purpose of further use of the wind tunnel at UiS.
It is important to note from this that all these calculated parameters have degrees of uncertainties to them.

2.7.4 Velocity throughout the test section

A increase in flow velocity occur throughout the test section as described in Section 2.2. The velocity is measured at the very beginning of the test section using either the pitot tube or the contraction, but the actual flow velocity at the position of the body under consideration is not known.

Assuming that the boundary layers remain laminar at all velocities, Equation (2.38) is used to find the boundary layer thickness at a distance from the beginning of the test section (x) [6]:

$$\delta = \frac{1.72x}{\sqrt{Re_x}} \tag{2.38}$$

Using the boundary layer thickness at the location of body (center of test section) to find the area of "free flow" at this point , the continuity equation (2.33) and the velocity at inlet, the velocity at the center of test section can be found [6]:

$$V_2 = \frac{A_1 V_1}{A_2} = \frac{0.45^2 V_1}{[0.45 - 2(\frac{1.72x}{\sqrt{Re_x}})]^2} \tag{2.39}$$

Table 6 shows all measured velocities (at the beginning of the test section) vs. calculated velocity at the test section center where bodies are mounted:

Table 6: Velocities measured at inlet vs. the calculated velocity at the test section center

Vel., inlet ($\mathrm{m\,s^{-1}}$)	Vel., center ($\mathrm{m\,s^{-1}}$)	Vel., inlet ($\mathrm{m\,s^{-1}}$)	Vel., center ($\mathrm{m\,s^{-1}}$)
1	1.037	23	23.174
2	2.052	24	24.178
3	3.064	25	25.182
4	4.073	26	26.185
5	5.082	27	27.189
6	6.089	28	28.192
7	7.097	29	29.195
8	8.103	30	30.199
9	9.109	31	31.202
10	10.115	32	32.205
11	11.121	33	33.208
12	12.126	34	34.212
13	13.131	35	35.215
14	14.136	36	36.218
15	15.141	37	37.221
16	16.145	38	38.224
17	17.150	39	39.226
18	18.154	40	40.229
19	19.158	41	41.232
20	20.162	42	42.235
21	21.166	43	43.238
22	22.170	43.5	43.739

3 Experimental and setup

3.1 Modifications

Since the wind tunnel is new there were some issues that needed to be improved. As result of this a part of the project was to design better solutions for testing and visualizing flow for future learning and experiments.

Support and dummy support for disks
To find the force acting on the disk in testing, the force acting on the support needs to be taken into account. We chose to use the image method where dummy supports are used to determine the force acting on the support and correcting the measured force acting on the disk. The image method is explained in Section 2.1.4. Two "identical" supports where fabricated out of 8mm stainless steel bar as can be seen in Figure 7.

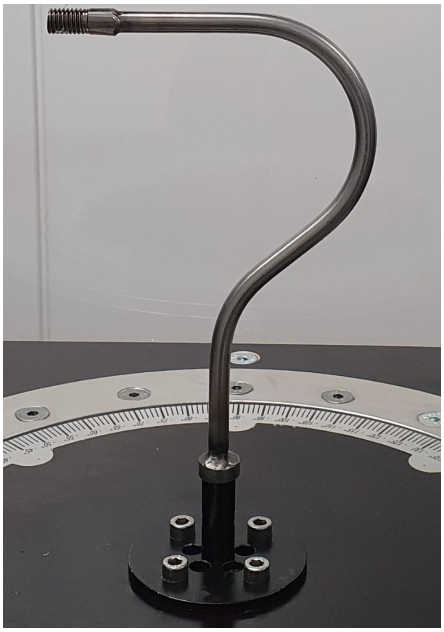

Figure 7: Fabricated support

To fasten the dummy support we needed to design a new roof for the test section as the original one is plain. We wanted to keep the original plate as it is, so the solution was to make a new plate with a lid with the same dimension as the one on the side plate so they can be used both places. Two lids were made; one with holes to fasten supports and one plain. We also added a support for the smoke generator using a cable gland to prevent air from leaking into the air stream and a transition from M20 to M16 with a small hole for supporting the smoke generator. See Figure 8.

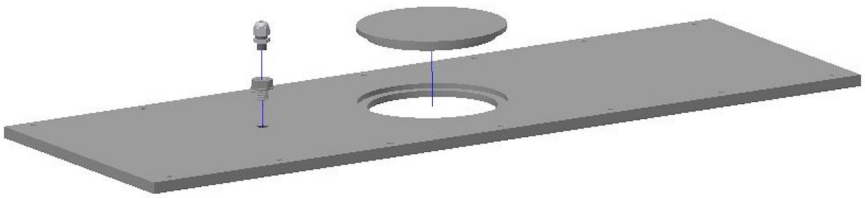

(a) Plate setup for smoke visualization

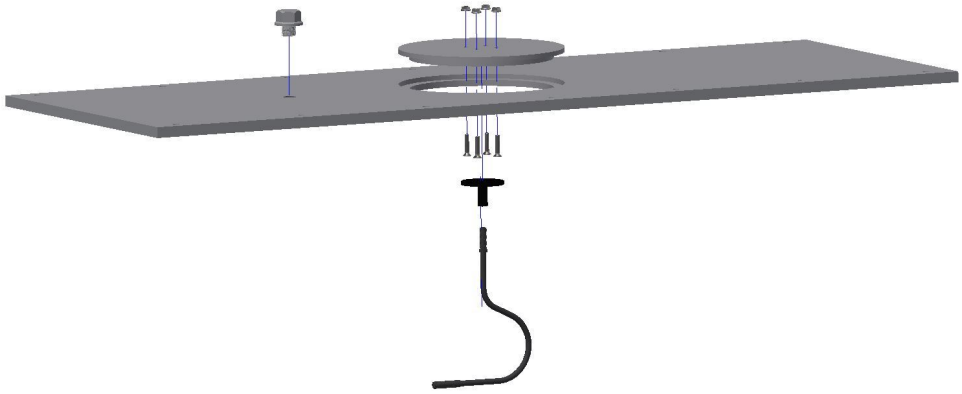

(b) Plate setup for disk test with dummy support

Figure 8: Exploded views of roof plate with different configurations

3.2 Circular disk

In this experiment, a total of four circular disks with diameters of 50, 100, 150 and 200mm was tested where the blockage ratios are 1%, 3.9%, 8.7%, 15.5% respectively (without the blockage of the supports). Each disk underwent three tests, as described in Section 2.1.4 using the image method. The first test involved only the disk and support. For the second test the dummy support was added but not connected to the disk itself. For the final test

the disk was mounted on the dummy support, without any contact to the actual support. See Figure 9.

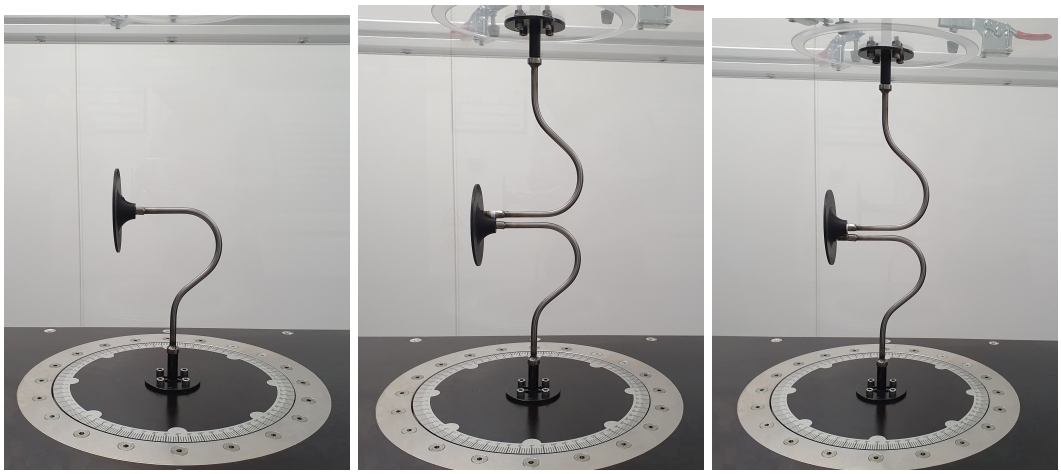

(a) Test 1 (b) Test 2 (c) Test 3

Figure 9: Test setups for disks

The velocity for each test ranged from $3\,\mathrm{m\,s^{-1}}$ to $25\,\mathrm{m\,s^{-1}}$ in increments of $1\,\mathrm{m\,s^{-1}}$. The wind velocity was held constant (to the best of our ability) for about 15 seconds at each velocity setting. The wind tunnel logger recorded data every second, resulting in approximately 15 data points per $\mathrm{m\,s^{-1}}$. However, due to the open wind tunnel configuration, the surrounding winds influenced the velocity, making it challenging to maintain a constant velocity in the tunnel.

Due to some complications using the image method (discussed further in the result section), a CFD simulation was done by our supervisor, Knut Erik Teigen Giljarhus to provide some additional indications of the force contribution that the support has on the measured force. A setup equal to Figure 9a was simulated at a velocity of $40\,\mathrm{m\,s^{-1}}$ with a disk diameter of 100mm.

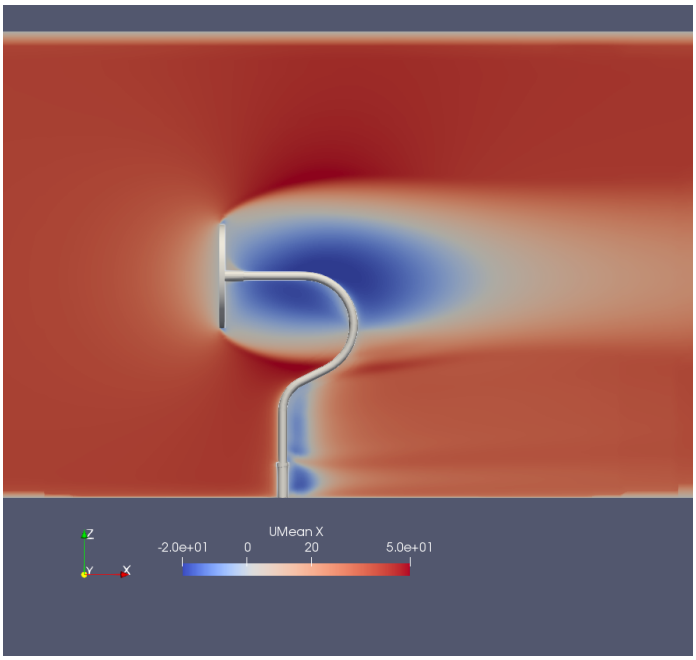

Figure 10: Velocity component in x direction (provided by K. E. T. Giljarhus)

Figure 10 displays the velocity component in the direction of flow (x-direction), revealing a low-velocity wake behind the disk that provides sheltering for some of the support from the high- velocity flow. Figure 11a shows the drag area on the support, which is determined by the product of the drag coefficient and frontal area. It is apparent from the figure that the majority of the force contributed by the support is concentrated on the straight part of the support located below the wake. This is further illustrated in Figure 11b, which shows the cumulative drag force along the height of the support, where the drag force tapers of at a height of approximately 0.1 m.

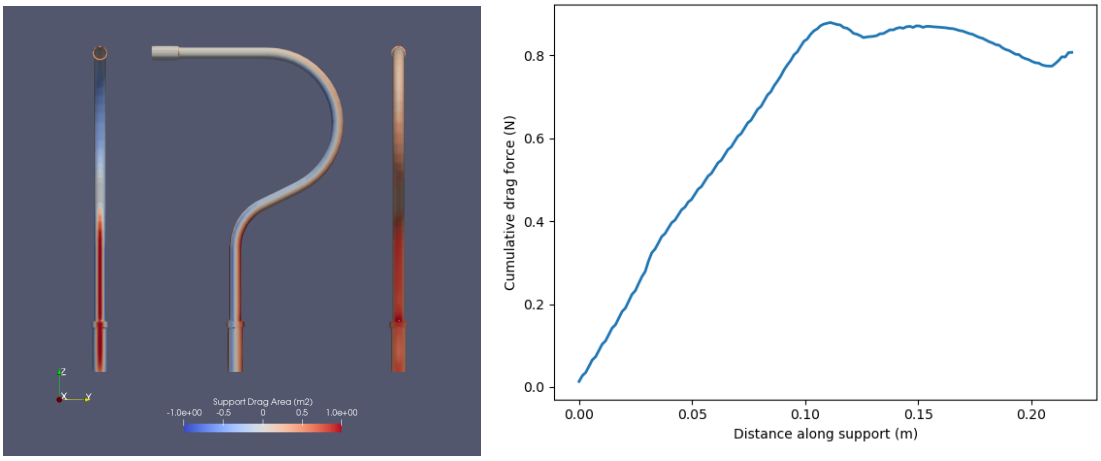

(a) Drag area of support

(b) Cumulative drag force on support

Figure 11: CFD simulations of 100mm disk at $40\,\mathrm{m\,s^{-1}}$ (provided by K. E. T. Giljarhus)

Using this length of 0.1 m, the support diameter and the cylinder drag coefficient at the relevant Reynolds number, it is possible to estimate the drag force contribution from the support at various velocities. For other disk diameters a new length would have to be determined.

3.3 Cylinder

A cylinder with diameter of 120 mm and a height of 230 mm was designed for the purpose of testing (see Figure 12b). The cylinder was equipped with 24 air channels around the circumference to measure surface pressure as can be seen in Figure 12a. The reason for the low aspect ratio (1.92) is to minimize the blockage effect (13.6%) but still be able to reach the transition region from laminar to turbulent boundary layer (see Section 2.4). The cylinder was drawn in Autodesk Inventor CAD-program and was resin printed at UiS. The tube connectors was ordered by UiS and manufactured by a third party.

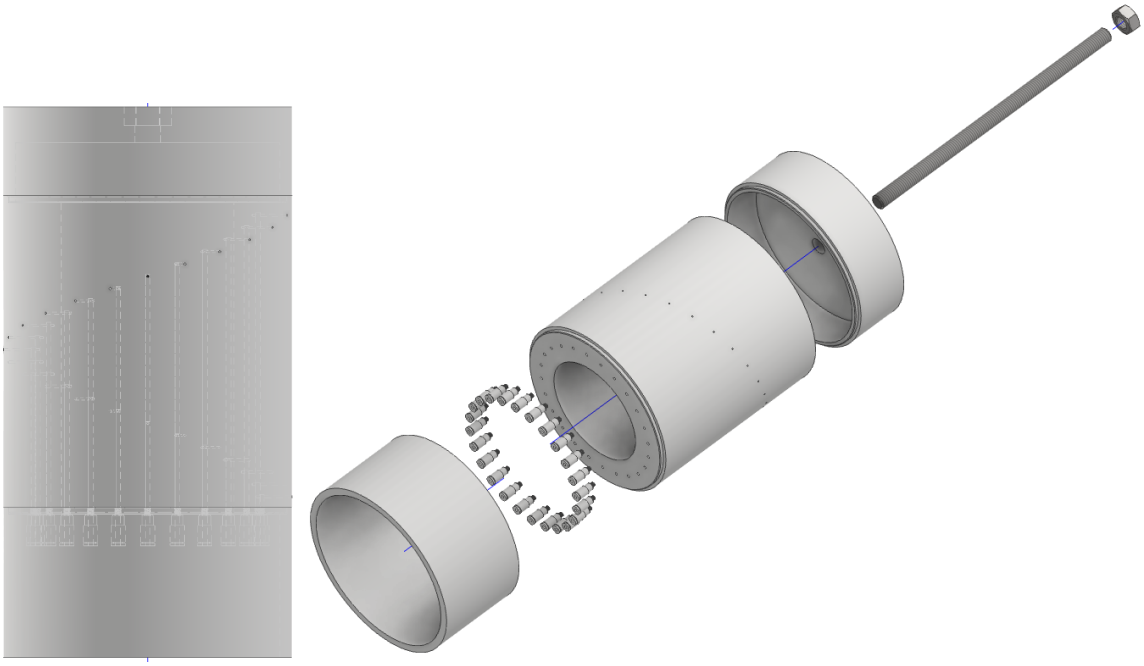

(a) Cylinder, assembled (b) Cylinder, exploded view

Figure 12: Designed cylinder for testing purpose

Several tests was performed on the cylinder, these was:

- Test from 3 to 43.2 $\mathrm{m\,s^{-1}}$ in increments of 1 $\mathrm{m\,s^{-1}}$, measuring forces
- Test at 15, 18, 30, 40 and 43.2 $\mathrm{m\,s^{-1}}$, measuring surface pressure.
- Visualisation of flow using smoke generator
- Visualisation of separation points using flow- viz paint

The flow- viz paint was mixed by using color pigment and Shell "Ondina" X 420 oil.

For the calculation of force using the surface pressure described in Section 2.7 the lower thirteen channels was used (assuming identical flow on each side then multiply result by two), where channel 1 faced the direction towards the flow with an angle of 0°and the channel 13 faced the direction of the flow (180°). The test velocities for surface pressure tests was chosen in the most interesting region, where the drag crisis occur but at 40 and 43.2 $\mathrm{m\,s^{-1}}$ the SVM-tec pressure scanner‘s range was maxed out.

3.4 Step cylinder

To compare drag coefficients on a step cylinder a total of three cylinders was designed in Autodesk Inventor CAD- program and FDM- printed in ABS-plastic at UiS. To minimize the effect of the free end on the results (discussed in Section 2.4), the height of each cylinder was set to 445mm, while the total height of the test section is 450mm. Although the clearance between the top of the cylinders and the roof of the test section could have been tighter and could possibly cause the free end to reach the boundary layer over and may have further minimized the effect. However, due to the properties of ABS-plastic the bending displacement is significant and some clearance is needed for it to not contact the test section roof.
The largest diameter was chosen to 60mm. This was mainly to not create a to large blockage effect for the 60mm dia. uniform cylinder (Figure 13a). Dimensions on a actual buoyancy element and cable was given to us [3] as 0.557 m and 0.116 m respectively. This results in a diameter ratio (D/d) of 4.8. With the diameter ratio the smaller diameter is found at 12.5mm. The step is at the midway of the cylinder length (222.5mm). The blockage effects of the 60mm dia. uniform cylinder, the 12.5 mm dia. uniform cylinder and the step cylinder is 13.2%, 2.7% and 8.0% respectively. The cylinders can bee seen in Figure 13. They are all split due to maximum print height on the printer used is lower than required height, and for the 60mm cylinder and step cylinder (see Figure 13a and 13c) it also enables us to hide the fastening bolts on the inside as seen in Figure 14.

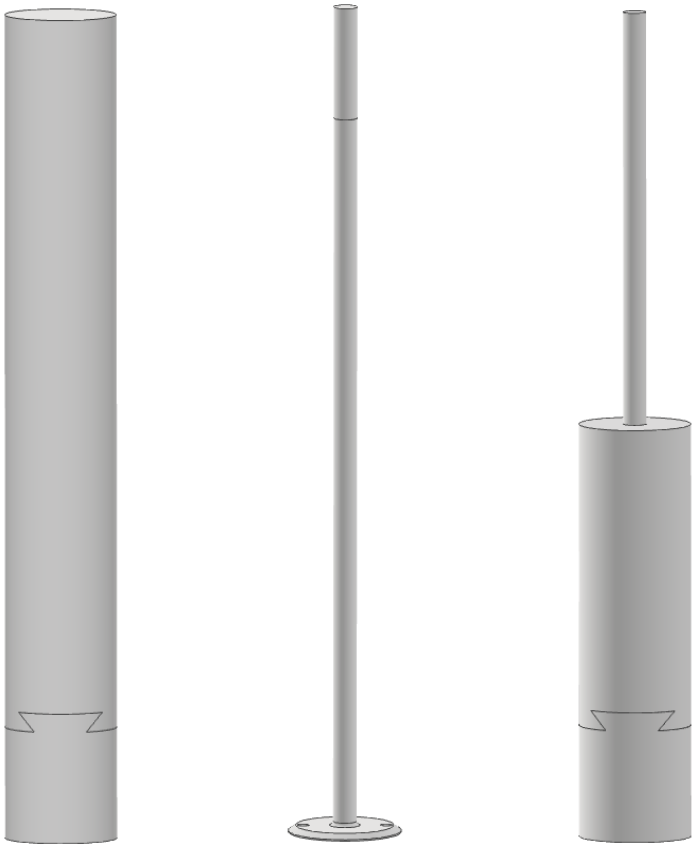

(a) Uniform 60mm dia. cylinder (b) Uniform 12.5mm dia. cylinder (c) step cylinder 60 and 12.5mm dia.

Figure 13: Designed cylinders and step cylinder for testing purpose

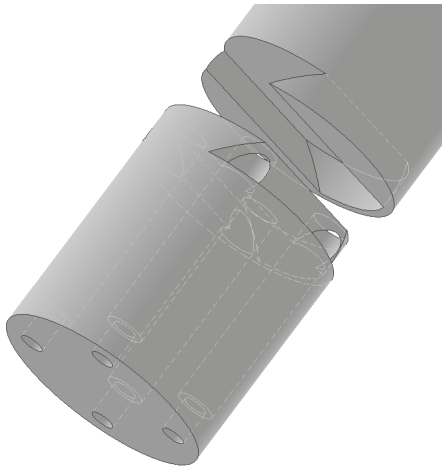

Figure 14: 60mm and step cylinder split detail, hiding fastening bolts

The 12.5mm cylinder in Figure 13b required a base-plate to fasten it securely to the measuring table in the test section. However, there was a concern that the stress at the junction of the base-plate and cylinder might be larger than yield strength of the ABS- plastic, where it could potentially break off and harm the fan.To address this concern, a (Von Mises) stress analysis was conducted in Autodesk Inventor CAD- program. The min. yield strength for ABS- plastic, which is 29.8MPa [39] was used as the benchmark. A force equal to the maximum expected load during testing was applied (10N at the mid way of the cylinder length). Figure 15a show a small red area where the stress is at 28.52MPa which was considered too close to the benchmark. Therefore, a radius was added to disperse the stresses from the concentrated corner, resulting in a maximum stress of 21.6MPa, as seen in Figure 15b.

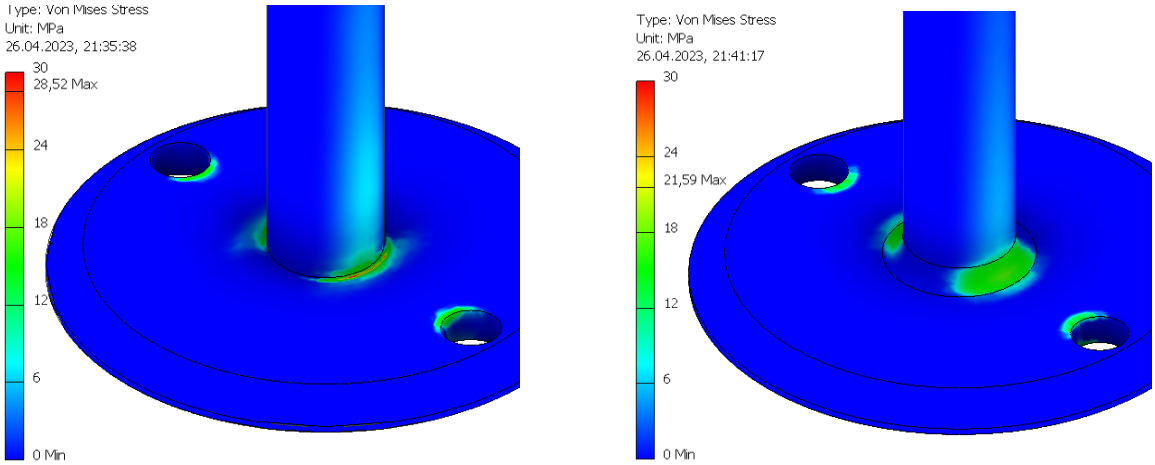

(a) Stress analysis without radius

(b) stress analysis with radius

Figure 15: Von Mises stress analysis on 12.5mm cylinder

All three cylinders were tested from 6 to 43 $\mathrm{m\,s^{-1}}$ in increments of 1 $\mathrm{m\,s^{-1}}$ and force data was collected. The reason for not considering lower velocities is due to the difficulties in keeping a constant velocity at this specific day (more info. in Section 5.1). The test setups for the three tests performed can be seen in Figure 16. It was desirable to test the step cylinder trough all achievable Reynolds numbers for the actual buoyancy element and cable (Re >1 000 000 for the 0.557 m diameter), but the blockage ratio limits us to this 60mm diameter, and the flow velocity is limited to about 43 $\mathrm{m\,s^{-1}}$ resulting in a maximum Reynolds number achieved at approx. 180 000 (for the 60mm diameter).

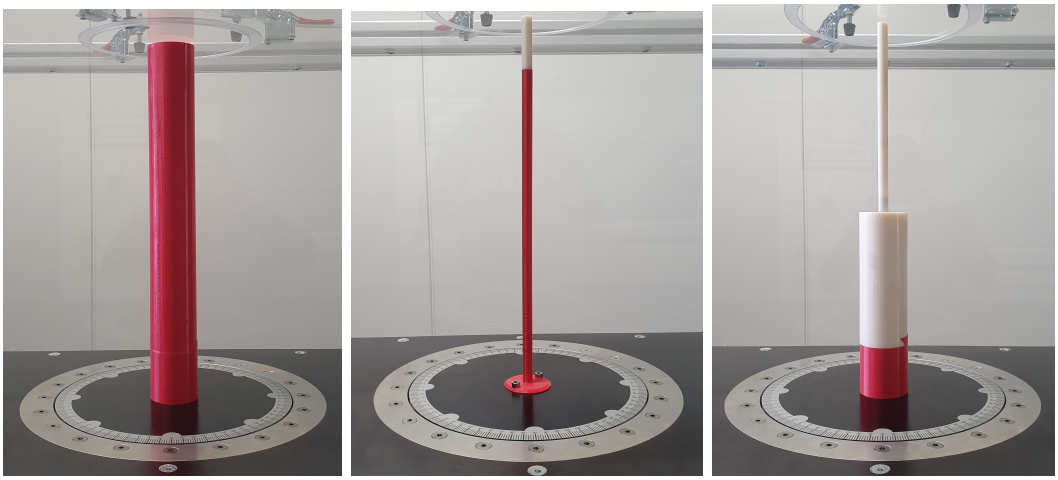

(a) Test setup, 60mm dia. uniform cylinder

(b) Test setup, 12.5mm dia. uniform cylinder

(c) Test setup, 60/ 12.5mm step cylinder

Figure 16: Test setups for tests considering step cylinder

Due to the flexible properties of the ABS- plastic, the bending displacement and general wobbling (most likely due to the vortex shedding) was severe for the 12.5mm dia. uniform cylinder at the highest flow velocities.

4 Results and discussion

To obtain the most accurate values of force using measuring table or pressure using SVM tec PSC24 scanner, more than 15 data-points was collected per $\mathrm{m\,s^{-1}}$ and averaged to reduce random error. All velocities have been corrected to calculated velocities at center of test section. This applies for all tests in this report.

4.1 Disks

In this section results from experiments on the circular disks is presented, compared and discussed.

The uncorrected and corrected drag coefficients for each disk is presented in Figure 17. Where the standard deviation of the retrieved data is shown on the uncorrected data. The uncorrected data have been corrected using the image method, but is referred to as uncorrected when comparing it to the blockage- correction methods.

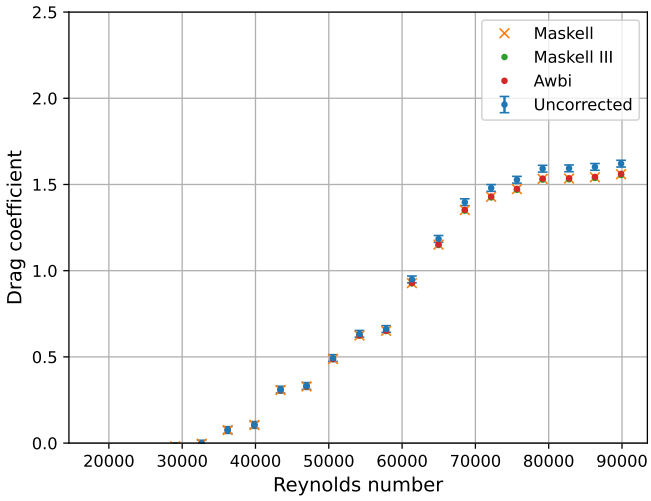

(a) 50mm disk

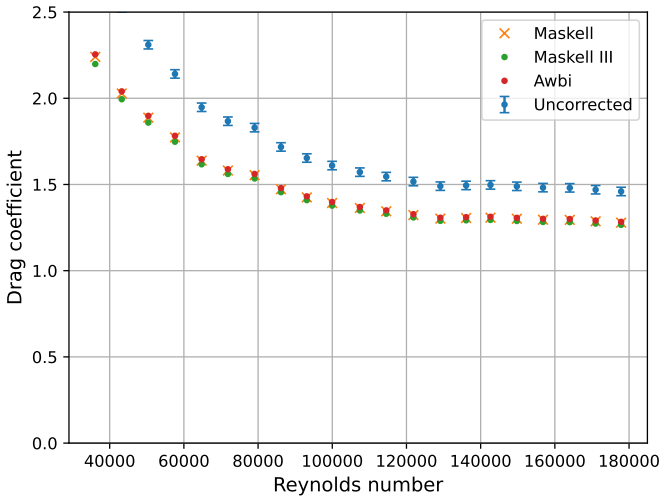

(b) 100mm disk

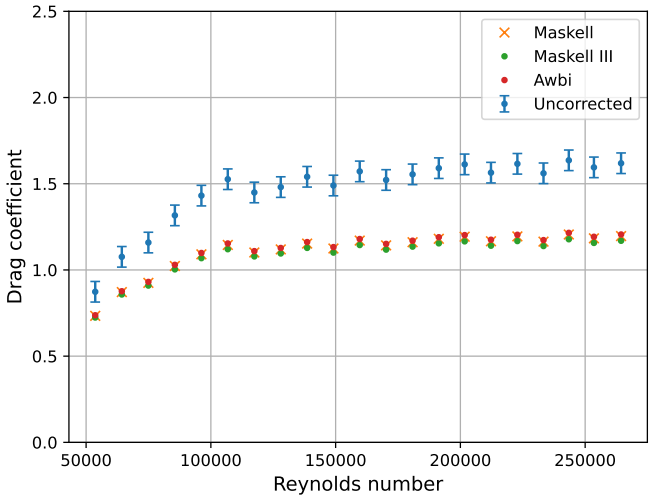

(c) 150mm disk

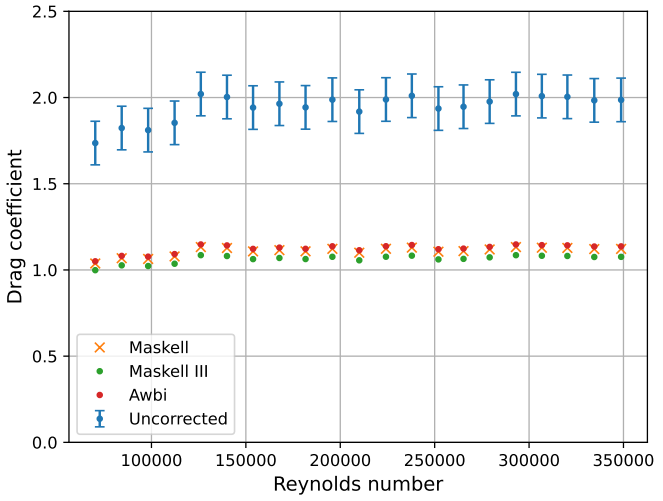

(d) 200mm disk

Figure 17: Uncorrected and blockage- corrected drag coefficients for each disk

The blockage- corrected drag coefficients using the three different methods shows close resemblance for all disks, where the Maskell III method gives a slightly lower drag coefficient overall. The difference between the uncorrected and corrected drag coefficients seem to be larger as the disk diameter increases.

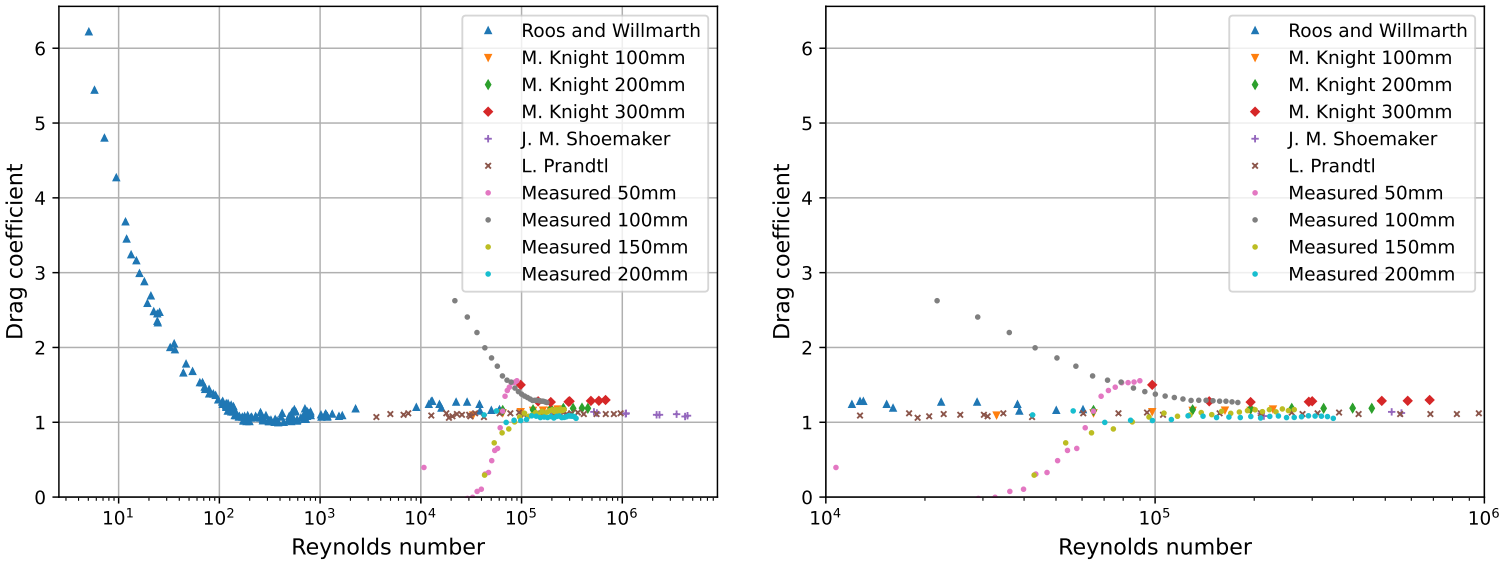

(a) Full range

(b) Relevant Reynolds number- range

Figure 18: Measured drag coefficients compared to drag coefficients from other studies

Figure 18a presents drag coefficients for circular flat disks from previous studies and blockage-corrected results from this study using the Maskell III method only due to the small variations in methods. More info. on the previous studies can be found in Section 2.3. Figure 18b presents the same data as Figure 18a but only in the region where results from this study are located for easier comparison. The corrected drag coefficients for the 200 and 150mm disk (at Re $>$ 100 000) seem to correspond well to the previous result. where as the 100 and 50mm disk show large deviations.

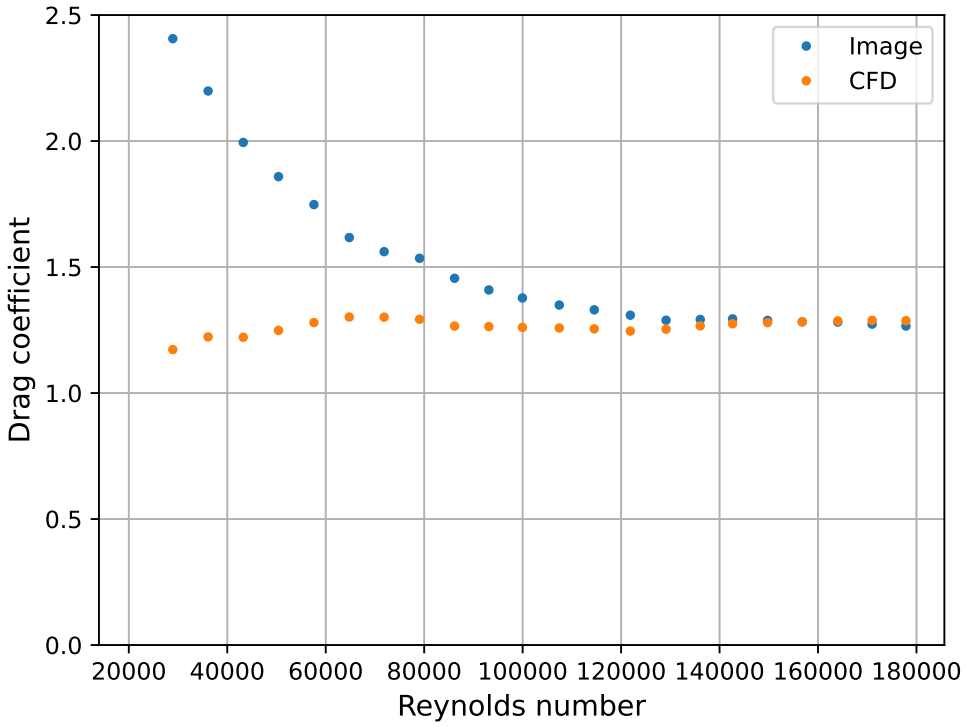

Figure 19: Comparison on drag coefficients for the 100mm disk by using the image method and by using support- results from CFD simulations (both are corrected using the Maskell III method)

A concern about the results generated by the image method was raised due to the large deviations in the corrected drag coefficients especially for the 100 and 50mm disk. Figure 19 shows a comparison on drag coefficient for the 100mm disk, using the image method and using results from CFD simulations to correct for support interference. The image method-corrected drag coefficient shows a decreasing trend that levels out at the end while the CFD-corrected drag coefficient is closer to constant.

4.1.1 Discussion, Circular disks

The theory suppose that at Reynolds numbers above 1000, the drag coefficient should be practically constant. The 200mm disk and the 150mm disk at Re $>$ 100 000 shows constant corrected drag coefficients. The 100mm disk coefficients seems to become close to constant at the highest Reynolds numbers, but the 50mm disks show little resemblance of a constant drag coefficient. The magnitude of the corrected drag coefficients, for where the coefficients are constant, seem to correspond well to previous results.

The magnitude of the corrections seem to naturally correspond to the blockage ratio as it should. The differences between the three blockage- correction methods themselves are difficult to further distinguish from one another. Even with the large blockage ratio for the 200mm disk, the correction methods seem to be relatively effective when comparing to previous results.

There seems to be something wrong with the image method applied to the data for the 100mm disk since the CFD- corrected drag coefficient is far closer to constant and corresponds to the magnitudes of previous results. this probably applies to the apparent deviations on the 50 and 150mm disk as well.

4.2 Cylinder

In this section results from experiments on the cylinder is presented, compared and discussed.

4.2.1 Drag coefficients and pressure distribution

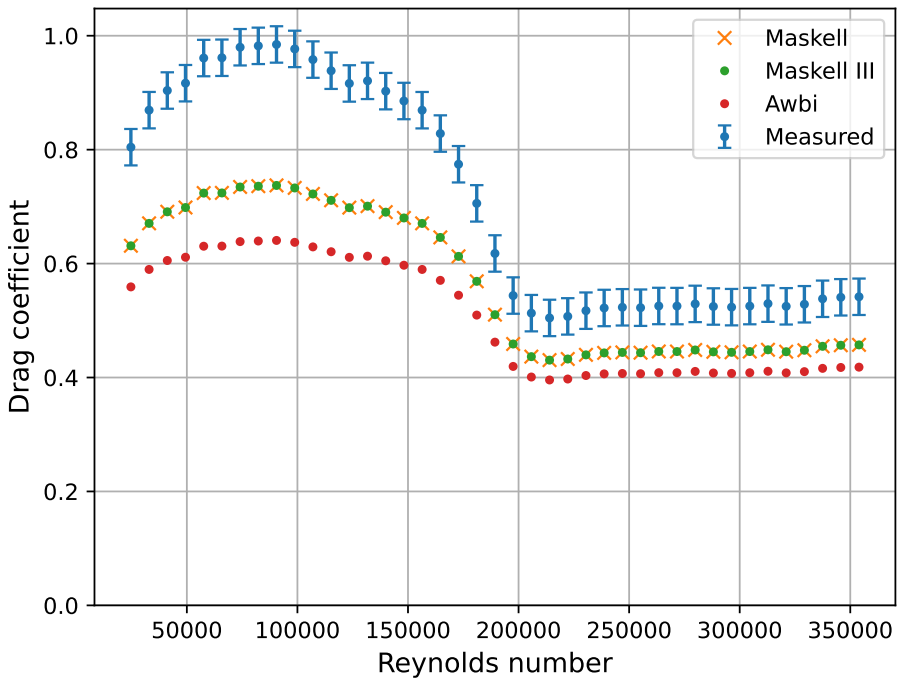

Figure 20: Uncorrected and corrected drag coefficients for 120mm dia. cylinder

The results on corrected and uncorrected drag coefficients in this study at different Reynolds numbers are presented in Figure 20 where the uncorrected drag coefficient shows the standard deviations from retrieved data. The magnitude of the corrections are significant. The Maskell III and Maskell's method seems to be close to identical, where Awbi's method resulted in a overall lower drag coefficient. For Awbi's method, the shape factor for range $0 < \frac{w_b}{h_b} \leq 0.5$ was used even though $\frac{w_b}{h_b} = 0.52$ for the cylinder under consideration.

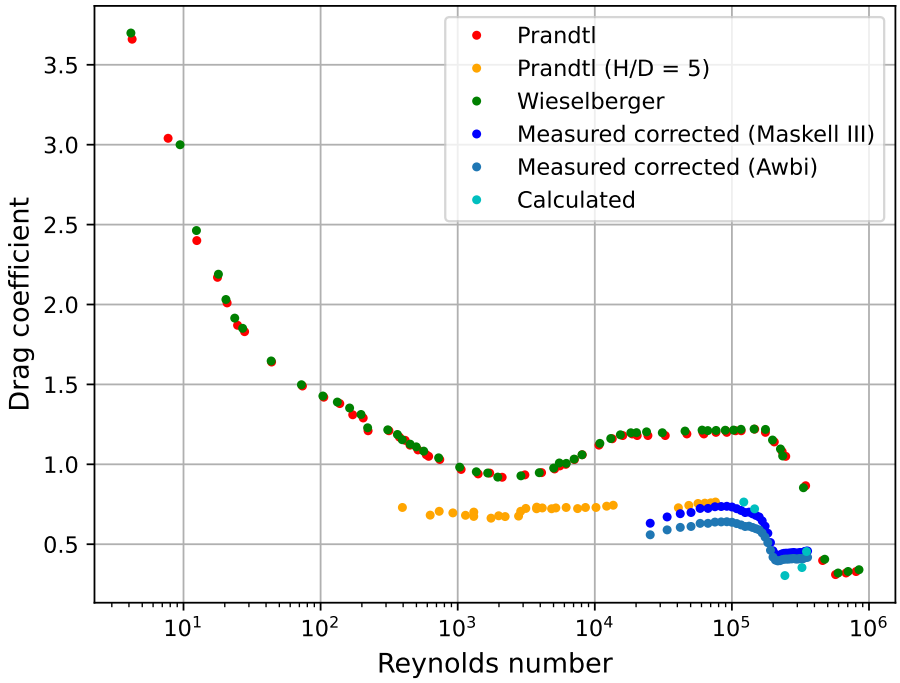

Figure 21: Measured C_D compared to other studies and C_D calculated using surface pressure

The drag coefficients from previous experiments on "two dimensional flow" and for the aspect ratio of 5, as well as results from experiments in this study (referred to as measured) and the calculated drag coefficients using the surface pressure (see Section 2.7) are plotted in Figure 21 for comparison.

The major drop in the corrected drag coefficients starting at Re $\approx$ 170 000 seems to correspond well to the previous results from Prandtl and Wieselberger on cylinders with "two dimensional" flow though our results seem to taper off earlier, at Re = 100 000, and the drop can be seen considerably smaller than for the previous results. Our results are also generally lower compared to results with "two dimensional" flow, but seem to better correspond to the test with aspect ratio of 5, where the Maskell III corrected drag coefficients are the most similar.
Results from calculating the drag coefficient corresponds to some degree with the measured results, where a decreasing trend similar to the measured results can be seen, though it seem to drop further before increasing again.

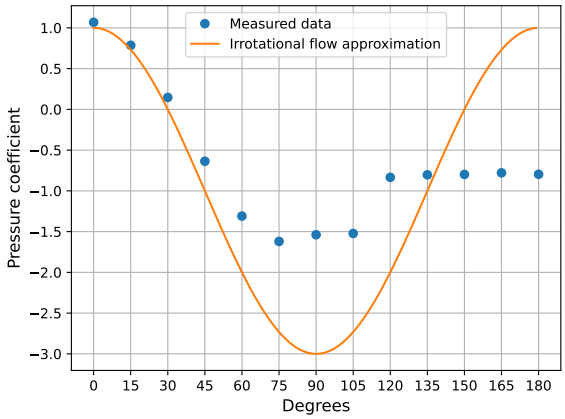

(a) Re = 120 000

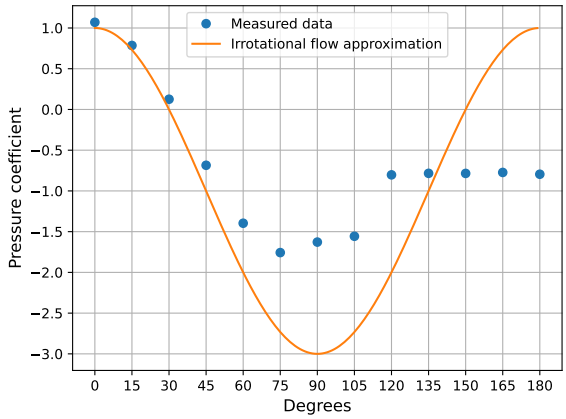

(b) Re = 151 000

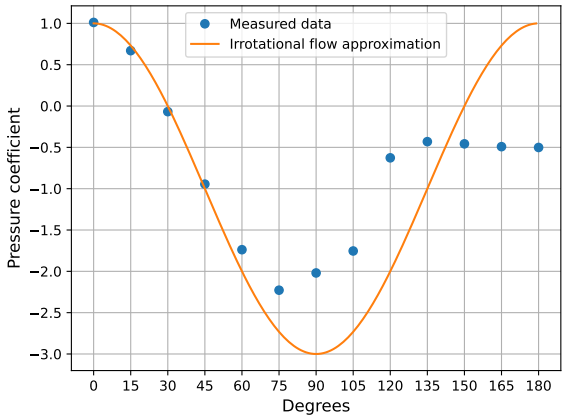

(c) Re = 250 000

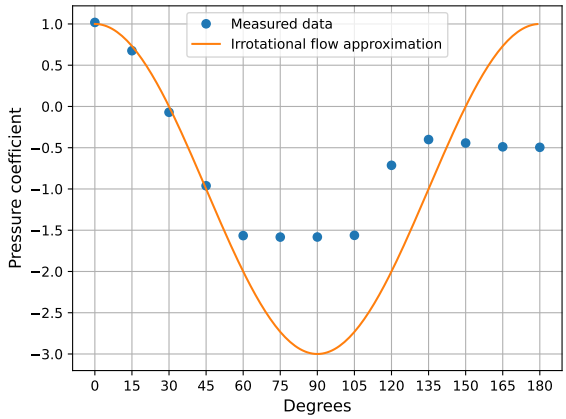

(d) Re = 330 000

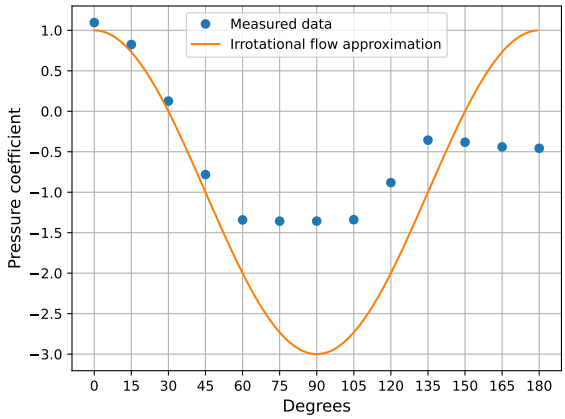

(e) Re = 362 000

Figure 22: Pressure coefficients compared at different Reynolds numbers

Figure 22 shows the pressure coefficients calculated using the surface pressures around the circumference of the cylinder at different Reynolds numbers compared to the irrotational flow approximation. The x- axis shows the angle at which the pressure is measured where 0°points straight towards the flow. Where the pressure coefficient becomes constant indicates that these points are all in the wake zone and that the separation occur right before this. Some development in the separation point angle can be seen throughout the Reynolds numbers. In Figure 22d and 22e the pressure coefficient seems to be constant from 60°to 105°.

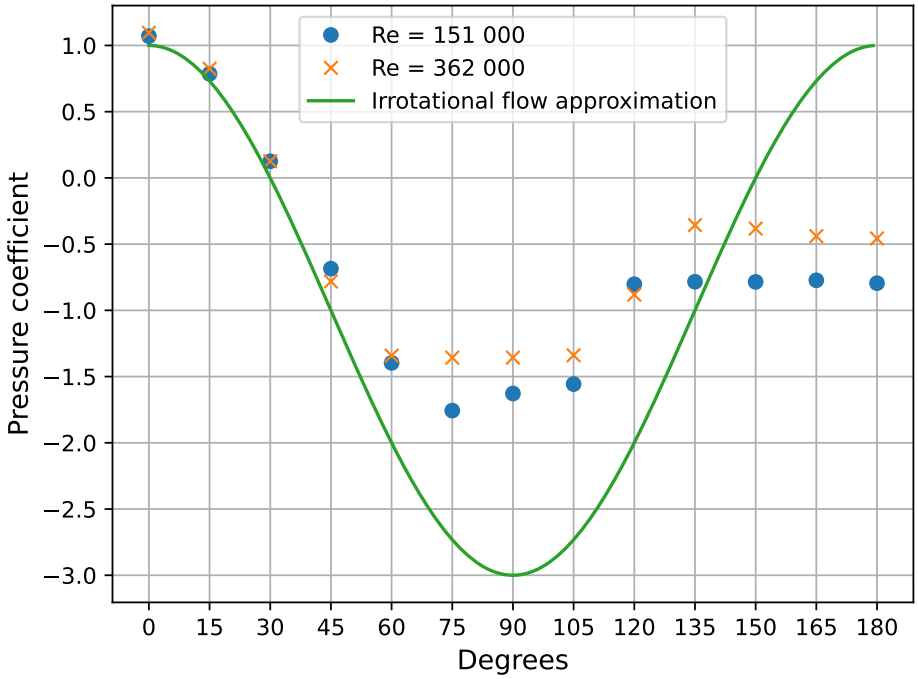

Figure 23: Pressure coefficients at laminar and turbulent boundary layer

In Figure 23 comparing the pressure distribution at laminar flow (Figure 22b) right before the drag crisis and after the drag crisis (Figure 22e) can be done.

The separation at Re = 151 000 seems to be at approx. 120°while the separation at Re = 362 000 is approx. 135°

4.2.2 Flow visualisation

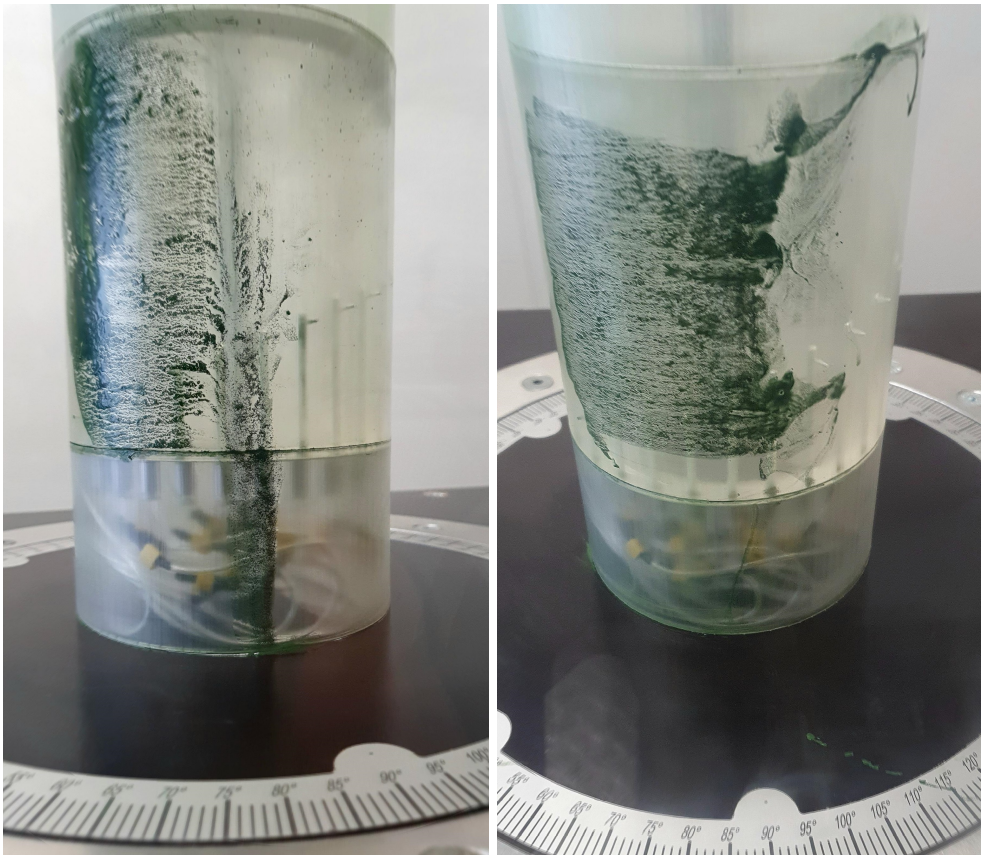

(a) Re = 151 000 (b) Re = 362 000

Figure 24: Flow viz paint tested on cylinder at two different Reynolds numbers.

The applied flow- viz paint can be seen in Figure 24. Where air flow passes the cylinder from left to right. At Re =151 000 (Figure 24a) where the boundary layer is assumed laminar, the paint seemed to pool up and start sagging downwards at about 80°, indicating that this is where the airflow separates. For Re = 362 000, the separation point can be estimated from the flow- viz paint at about 105°. A trailing tail can be seen in Figure 24b, close to the top of the cylinder running towards the back and slightly upwards.

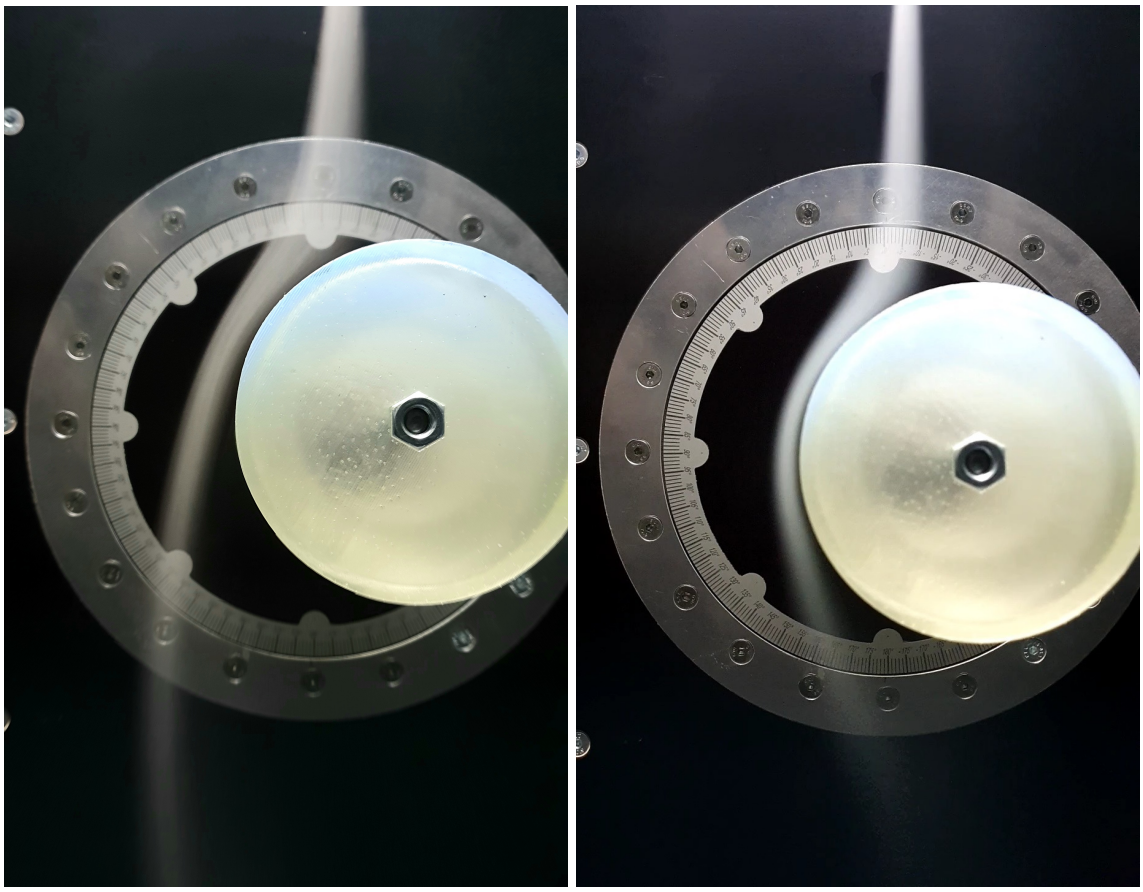

(a) Re = 151 000 (b) Re = 362 000

Figure 25: Smoke added to airflow past cylinder at two different Reynolds numbers (seen from above).

Smoke was applied to the airflow to visualise the flow past the cylinder at two different Reynolds numbers, referring to Figure 25. This test shows a clear difference in the two separation- point angles. From Figure 25a, a separation point slightly on the front side at approx. 80°with a wide wake can be seen. On Figure 25b the airflow follows the contour of the cylinder further towards the back to a separation point at approx. 115°.

4.2.3 Discussion, Cylinder

The clear drop in drag coefficients in Figure 20 at around Re = 170 000 can be attributed to the drag crisis effect. The large difference in uncorrected and corrected drag coefficients in Figure 20 is likely due to the large blockage effect that the cylinder has. The Awbi's corrected drag coefficients are generally lower than the two others. The shape factor that is included in Awbi's method is most likely the reason since this is the only difference compared

to Maskell's method. The use of a shape factor in Awbi's method, where the cylinder width to height ratio is just outside the range might have influenced the correction to an unknown extent.

The generally lower measured and calculated drag coefficients compared to previous results are assumed to be a result of the flow over the free end, creating higher base pressure in this region compared to a cylinder with "two dimensional flow". The magnitude of the drag coefficients from this study seems to correspond better to the results from the cylinder with aspect ratio of 5 where this effect also is present. The large blockage ratio, even when corrected could also contribute to some deviations.

The calculated drag coefficients at Re = 330 000 and 362 000 are not correct due to the pressure scanners range is maxed out. More data-points in the lower region could have been calculated to sufficiently compare. Some inaccuracy in the integration method is also expected, but wont be of a significant magnitude so this is neglected.

The laminar separation points from the flow- wiz visualisation and smoke visualisation at Re = 151 000 seems to correspond well with each other and with the theory at approx. 80°. The plotted pressure coefficient at Re = 151 000 however, indicates a separation later at approx. 120°. The separation point from the flow-wiz and smoke visualisation for Re = 362 000 show a small difference, but neither is close to the 140°separation point for turbulent boundary layer discussed in Section 2.4. The plotted pressure coefficient at Re = 362 000 however, indicates a separation point later at 135°which corresponds much better to the theory.

To determine the separation points from the flow visualisations can not be done accurately. The viscosity of the flow- viz paint can cause it stop before the actual separation point. From Figure 24a and 24b it is also clear that determining a separation point from the flow-viz paint is difficult. For the smoke visualisation, lighting and the amount of smoke added can influence where the separation seems to be. The late separation point from the plotted pressure coefficient at Re = 151 000 indicates that the boundary layer might already be in the transitional region though it does not seem like it from the flow visualisation tests. Another thing to note is that the tube connector threads for the surface pressure measurements do not have any additional tread seal applied, leaving a possibility that the treads might leak and give faulty results.

The trialing tail seen in Figure 24b is believed to be a result of the free end effect or the boundary layer of the "floor" where the cylinder is mounted to, creating some three dimensional flow.

4.3 Step cylinder

In this section the results from the experiments considering the step cylinder are presented and discussed.

Due to the large size difference in the two uniform cylinders the and the limited flow velocity, the Reynolds number ranges for the two barely overlaps and can not be compared to the step cylinder directly as can be seen in Figure 26.

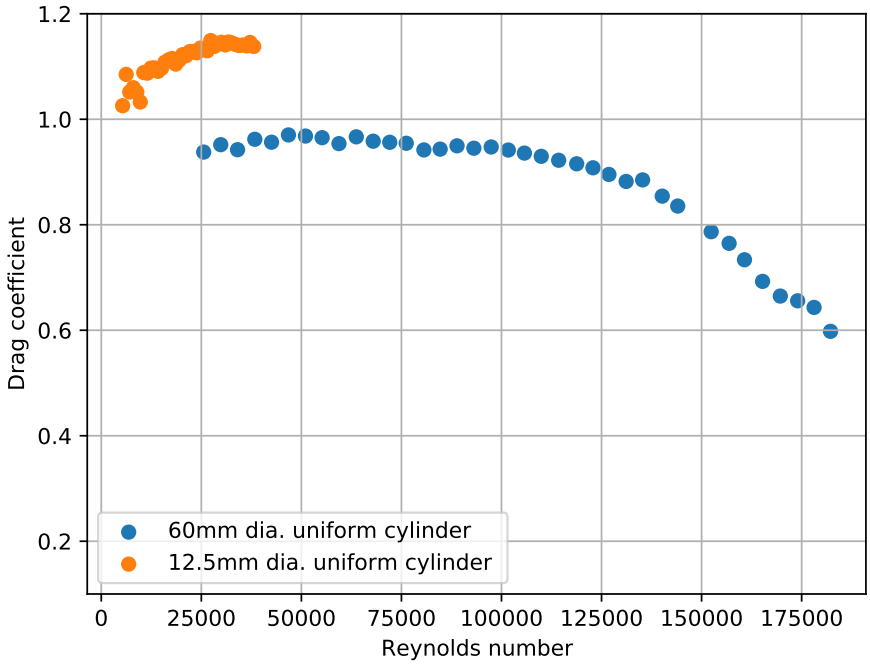

Figure 26: Drag coefficients for 60 and 12.5mm dia. uniform cylinders (both corrected using the Maskell III method)

In order to compare the step cylinder to the uniform cylinders and to see the effects that the step has on the drag coefficient, half the drag force of the 60mm dia. uniform cylinder and half the drag force of the 12.5mm dia. uniform cylinder where summed for each flow velocity and used for further calculating the drag coefficients. The combination of the two uniform cylinders is referred to as "Merged uniform cylinders".

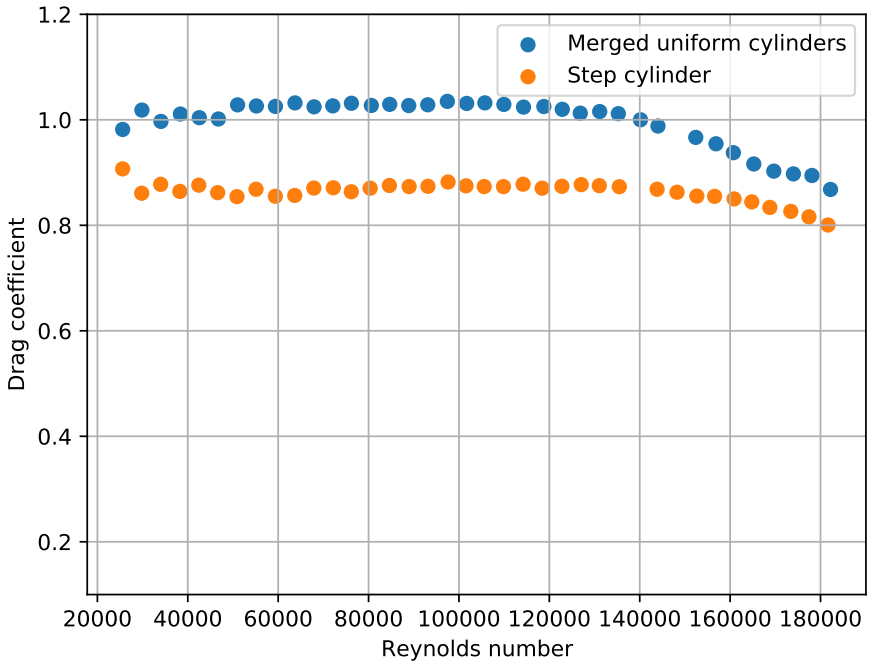

Figure 27: Drag coefficients for step cylinder and the merged uniform cylinders (both corrected using the Maskell III method)

The results for the step cylinder and the merged uniform cylinders are plotted in Figure 27. The Reynolds numbers are calculated using the 60mm diameter. The plot shows clearly a lower drag coefficient for the step cylinder compared to the merged uniform cylinders in this Reynolds number interval. No data was collected at the specific velocities of $33\,\mathrm{m\,s^{-1}}$ for the step cylinder (Re = 140 000) and $35\,\mathrm{m\,s^{-1}}$ for the uniform cylinders (Re = 150 000). Due to the wind tunnel velocity display freezes in this region and these velocities where missed (more info. in Section 5.1).

4.3.1 Discussion, Step cylinder

The primary reason for the step cylinder's overall lower drag coefficient, when compared to the merged uniform cylinders, can be attributed to an effect similar to the free end effect. This occurs because the flow over the step that does not interfere with the 12.5mm diameter part of the step cylinder, creates higher pressure on the backside of the 60mm diameter part. This means that there is a higher pressure on the backside of the step cylinder compared to what the uniform cylinders have. For smaller diameter ratios, this difference is most likely smaller. The significant bending displacement and general wobbling of the 12.5mm dia. uniform cylinder might have caused some further deviations in the results.

5 General discussion

Our limited prior knowledge of wind tunnel testing and aerodynamics in general resulted in a significant amount of time that had to be dedicated to learning and understand these subjects. Moreover, the original objective of the thesis was to gain experience in the use of the new wind tunnel. However, a significant amount of time had to be spent on unforeseen modifications to the wind tunnel that had to be made before the planned tests could be carried out. The modification aspect included designing, ordering parts from third parties, delivery times and installing of parts. Additionally, due to a backlog on the university 3D printers, it took longer than expected to print the test objects.
Taken together, this reduced the amount of time available for conducting tests and analysing the resulting data.

The uncertainty for calculated velocities using pitot tube or contraction shown in Table 5 is large, especially at the lower velocities. That means that values for Reynolds numbers, pressure coefficients and drag coefficients in this region carries a large uncertainty as well.

Some uncertainty in the calculated velocity throughout the test section is also expected but it is likely more accurate than only using the velocity at the inlet. The velocity increase throughout the test section could also be measured by somehow designing a movable pitot tube.

All three blockage- correction methods used on results seem to be effective in correcting drag coefficients. To decide which one is the most accurate is difficult with the limited results. To gain the most accurate results overall, testing at the lowest blockage ratio possible is probably a good rule of thumb.

5.1 Important practical notes

During testing and experimental work, we noted some important things to consider when conducting tests in the wind tunnel:

- Due to its open circuit design, the flow velocity is difficult to keep constant when there is a any sort of surrounding breeze, especially at lower flow velocities.
- After the test- body is mounted and before the fan is started, it is important to zero out the forces on the measuring table, but due to the open circuit design, it was experienced that the surrounding breeze created a flow trough the tunnel, in either direction. If the forces where to be zeroed out when there is a flow velocity trough the tunnel, the overall data could be offset from the true data.
- The same as for the measuring table goes for the SVM tec pressure scanner, it is important to zero out the pressures when flow velocity is $0\,\mathrm{m\,s^{-1}}$ to get the true data.

- The flow velocity shown on the tunnel display seem to lag/ freeze at around $32\,\mathrm{m\,s^{-1}}$ to $35\,\mathrm{m\,s^{-1}}$, The logged data doesn't seem to be affected by this but testing in this region is done somewhat blindly.

6 Conclusion

In this project the aerodynamics of circular disks, cylinders and step cylinder have been studied. The subject of the thesis is wind tunnel testing in the new wind tunnel at UiS. The overall goal was to gain confidence in wind tunnel testing and compare results to other studies on these objects. The project also included the use of blockage- correction methods and other methods. Before tests could be carried out, modifications of the wind tunnel and components to perform the tests planned had to be done. A new cylinder with pressure ports and the step cylinder had to be designed and 3D- printed. Also the "roof" of the wind tunnel test section had to be modified to be able to perform the tests considering the mirror correction method. The theory is explained in Section 2.

The blockage- correction methods (Maskell's, Maskell III and Awbi's method) for the disk results where the drag coefficients are constant all seem to give drag coefficients in close region to previous results where the differences are to small to conclude with the most accurate one. The large deviations on the 50mm and 100mm disk is due to unknown faults in the use of image the method.

Results on the cylinders corrected drag coefficients using the Maskell III and Awbi's method at different Reynolds numbers compared to previous results shows both similarities in the sudden reduction (drop) in drag coefficient at Re $\approx$170 000, but due to the free end effect the drag coefficients are lower overall with a smaller drop. The magnitude of the corrected drag coefficients from this study seems to correspond better to the results from the cylinder with aspect ratio of 5, further showing that the free end effect is why the generally lower drag coefficient. Where the Maskell III corrected drag coefficients is the most similar.

Conclude on the most accurate blockage- correction method can not be done with our limited results where all seem effective to some degree. However it can be assumed that the Maskell III is more accurate than Maskell's method since it also considers the wake distortion.

The calculated drag coefficients using the surface pressure are also generally lower than for the coefficients with "two dimensional" flow where these results are affected by the free end as well. There are closer similarities to the corrected drag coefficient from this study and a clear drop in the region showing that to calculate the drag coefficients can also be done with a somewhat satisfying accuracy. Results from where the pressure scanner is maxed out cannot be considered.

The comparison of drag coefficients for the step cylinder and merged uniform cylinders of the same diameters shows that, in this Reynolds number- range, calculating drag forces and drag coefficient can not be done accurately by only calculating together forces and coefficients from "two dimensional flow". The drag coefficient for a step cylinder will most likely be lower overall, where the difference depends on the diameter ratios.

Testing in the lower velocity region should be avoided if possible to retrieve data with

minimal uncertainties. It should at least be taken into consideration when testing in this region.

6.1 Future work

The following suggests some topics for future study on the specific wind tunnel, methods described and geometries tested in this report.

- Further investigate the uncertainties for parameters (drag coefficients Reynolds number, pressure coefficients, etc.) that uses the calculated velocity from the pitot tube or contraction.
- Further study the image method to fully understand why the data retrieved from this method deviates to other experiments and the CFD simulation.
- Measure the actual increase of flow velocity throughout the test section, for instance by designing a movable pitot tube, and compare it to the calculated velocity increase.
- Investigate the repeatability of the wind tunnel under the same test conditions would also be relevant for further use.
- Study the use of end plates to create "two dimensional" flow around the cylinder and compare results to previous results and the results in this report.
- Compare more blockage- corrected results from the wind tunnel to CFD simulations to further evaluate the blockage- correction methods.

References

[1] E.C. Maskell. A theory of the blockage effects on bluff bodies and stalled wings in a closed wind tunnel. Technical report, Her majesty‘s stationery Office, Kingsway, London, 1963.

[2] L. Prandtl. Ergebnisse der aerodynamischen versuchsanstalt zu göttingen. Technical report, University of Göttingen, 1923.

[3] Anja Schnepf. private communication, March 2023.

[4] Josué Njock Libii. Using wind tunnel tests to study pressure distributions around a bluff body: the case of a circular cylinder. https://core.ac.uk/download/pdf/47229541.pdf, 2010. [Online; accessed 23-January-2023].

[5] John M. Cimbala Yungus A. Cengel and Afshin J. Ghajar. *Fundamentals of thermal-fluid Sciences, sixth edition.* McGraw Hill LLC, New York, NY, 2022.

[6] Yungus A. Cengel and John M. Cimbala. *Fluid mechanics: Fundamentals and applications, Third edition.* McGraw Hill, New York, NY, 2014.

[7] Richard Shelquist. An introduction to air density and density altitude calculations. https://wahiduddin.net/calc/density_altitude.htm, 1998. [Online; accessed 23-January-2023].

[8] John M. Cimbala Yungus A. Cengel and Robert Turner. *Fundamentals of thermal-fluid Sciences, fifth edition.* McGraw Hill Asia, New York, NY, 2020.

[9] John Anderson. Sleeker and faster: The impact of the full scale wind tunnel. https://airandspace.si.edu/stories/editorial/sleeker-and-faster-impact-full-scale-wind-tunnel, 2020. [Online; accessed 14-May-2023].

[10] William H. Rae Jr. Jewel B. Barlow and Alan Pope. *Low speed wind tunnel testing.* John Wiley & sons, 1999.

[11] J.A Lawford R. Fail and R. C. W. Eyre. Low-speed experiments on the wake characteristics of flat plates normal to an air stream. Technical report, Her majesty‘s stationery Office, Kingsway, London, 1959.

[12] J. E. Hackett and K. R. Cooper. Extensions to maskell's theory for blockage effects on bluff bodies in a closed wind tunnel. *The Aeronautical Journal,*, 105(1050):409–418, 2001.

[13] Kevin Cooper, Miroslav Mokry, and Mark Gleason. The two-variable boundary-interference correction applied to automotive aerodynamic data. *SAE Technical Papers*, 04 2008.

[14] H.B. Awbi. *The investigation of wind tunnel wall interference on bluff-body models.* PhD thesis, Nottingham Trent University, 1974.

[15] Usama Bin-Khalid and Jenő Suda. Comparative study of wind tunnel blockage correction methods for bluff body aerodynamics (swimmer's hand model). 07 2020.

[16] Sighard F. Hoerner. *Fluid-dynamic drag*. Published by the Author, 1965.

[17] D.J Craze. *The near wake behind a circular disc in a smooth and turbulent airstream*. PhD thesis, University of Western Ontario, Canada, 1974.

[18] F. W. Roos and W. W. Willmarth. Some experimental results on sphere and disk drag. *AIAA*, 9(2):285–291, 1971.

[19] M. Knight. Wind tunnel standardization disk drag. Technical report, Langley Memorial Aeronautical Laboratory, 1926.

[20] J. M. Shoemaker. Resistance of a fifteen- centimeter disk. Technical report, Langley Memorial Aeronautical Laboratory, 1926.

[21] C. Wieselsberger. New data on the laws of fluid resistance. Technical report, NACA, TM no. 84, 1922.

[22] O. Güven, C. Farell, and V. C. Patel. Surface-roughness effects on the mean flow past circular cylinders. *Journal of Fluid Mechanics*, 98(4):673–701, 1980.

[23] Wenyong Ma, Bocheng Huang, Deqian Zheng, Meng Lu, and Haiyun Li. Effect of the presence of end plates and aspect ratio on the aerodynamic forces on circular cylinders in various flow regimes. *Fluid Dynamics Research*, 51(5):1–21, 2019.

[24] Cheol-Woo Park and Sang-Joon Lee. Free end effects on the near wake flow structure behind a finite circular cylinder. *Journal of Wind Engineering and Industrial Aerodynamics*, 88(2):231–246, 2000. International Conference on wind Engineering.

[25] P. K. Stansby. The effects of end plates on the base pressure coefficient of a circular cylinder. *The Aeronautical Journal*, 78(757):36–37, 1974.

[26] T. A. Fox and G. S. West. On the use of end plates with circular cylinders. *Experiments in Fluids*, 9:237–239, 1990.

[27] ZHENG Yun-fei, LIU Qing-kuan, LIU Xiao-bing, and MA Wen-yong. Influence of end conditions on aerodynamic force of section models for stay-cables. *Engineering Mechanics*, 34(2017S133):192–196, 2017.

[28] Peter A. Irwin. Vortices and tall buildings: A recipe for resonance. *Physics Today*, 63(9):68–69, 09 2010.

[29] Bengt Sunden. Vortex shedding. https://www.thermopedia.com/content/1247/, 2011. [Online; accessed 11-May-2023].

[30] N. W. M. Ko and A. S. K. Chan. In the intermixing region behind circular cylinders with stepwise change of the diameter. *Experiments in Fluids*, 9:213–221, 1990.

[31] Tian Cai, Fengjian Jiang, Bjornar Pettersen, and Helge Andersson. Numerical investigation of flow around a step cylinder. 05 2017.

[32] K. Twarowska . *University of Stavanger Subsonic wind tunnel in 40 ft. container*. CTO S.A, 65 Szczecińska St. 80-392 Gdańsk, Poland, 2022.

[33] L. Prandtl. Attaining a steady stream in wind tunnels. Technical report, NACA, TM no. 726, 1933.

[34] Next Thermal. Different range of temperature sensors in accuracy and responsiveness. https://www.nexthermal.com/different-range-of-temperature-sensors-in-accuracy-and-responsiveness/#:~:text=Temperature%20sensor%20accuracy%20is%20critical,1%C2%B0C%20for%20most. [Online; accessed 26-April-2023].

[35] Department of civil enviromental & geomatic engineering. Pressure around a cylinder and cylinder drag, 1998. [Online; accessed 13-March-2023].

[36] B. S. Massey and J. Ward-Smith. *Mechanics of Fluids*. Taylor & Francis, 2. Park Square, Milton Park, Abingdon, Oxon OX14 4RN, eighth edition, 2006.

[37] K. Nawacki. private communication, march 2023.

[38] European Accreditation. Evaluation of the uncertainty of measurement in calibration. https://european-accreditation.org/publications/ea-4-02-m/, April 2022. [Online; accessed 15-April-2023].

[39] Omnexus. Comprehensive guide on acrylonitrile butadiene styrene (abs). https://omnexus.specialchem.com/selection-guide/acrylonitrile-butadiene-styrene-abs-plastic. [Online; accessed 26-April-2023].

Appendix A

The appendix A includes Safety data sheet for Shell Ondina X 420 oil used for flow-viz paint and smoke generator as well as Fixor Pigment Kromoxidgrön (Pigment chromeumoxside-green) used for flow-viz paint.

Note: The safety data sheet for Shell Ondina X 420 is sourced from the manufacturer/supplier Shell UK Oil Products Limited and can be found at url: http://triska-uploads.s3.amazonaws.com/1481027848-MSDS_Ondina_X_420.pdf.

The safety data sheet for Pigment Kromoxidgrön (Pigment chromeumoxside- green) is sourced from the manufacturer/supplier AB Alfort & Cronholm and can be found at url: https://www.bauhaus.no/media/pdf/5007328A_SDS.pdf.

SECTION 1: Identification of the substance/mixture and of the company/undertaking

1.1 Product identifier

Trade name	:	Ondina X 420
Product code	:	001E2771
Registration number	:	01-0000020163-82-0001
CAS-No.	:	1262661-88-0

1.2 Relevant identified uses of the substance or mixture and uses advised against

Use of the Substance/Mixture	:	Process oil. Please refer to Ch16 for the registered uses under REACH.
Uses advised against	:	This product must not be used in applications other than those listed in Section 1 without first seeking the advice of the supplier.

1.3 Details of the supplier of the safety data sheet

Manufacturer/Supplier	:	**Shell UK Oil Products Limited** Shell Centre London SE1 7NA United Kingdom
Telephone	:	(+44) 08007318888
Telefax	:	
Email Contact for Safety Data Sheet	:	If you have any enquiries about the content of this SDS please email lubricantSDS@shell.com

1.4 Emergency telephone number
: +44-(0) 151-350-4595

SECTION 2: Hazards identification

2.1 Classification of the substance or mixture

Classification (REGULATION (EC) No 1272/2008)

Aspiration hazard, Category 1	H304: May be fatal if swallowed and enters airways.

2.2 Label elements

Labelling (REGULATION (EC) No 1272/2008)

SÄKERHETSDATABLAD

Enligt 1907/2006 bilaga II och 1272/2008
(Alla hänvisningar till EU-förordningar och direktiv är förkortade till endast nummerbeteckningen)
Revisionsdatum 2021-02-26
Ersätter blad utfärdat 2021-02-26
Versionsnummer 6.0

AVSNITT 1: Namnet på ämnet/blandningen och bolaget/företaget

1.1 Produktbeteckning

Handelsnamn	Pigment Kromoxidgrön
Artikelnummer	226546, 291865, 288570

1.2 Relevanta identifierade användningar av ämnet eller blandningen och användningar som det avråds från

Identifierade användningar	Pigment för färger

1.3 Närmare upplysningar om den som tillhandahåller säkerhetsdatablad

Företag	AB Alfort & Cronholm Box 110 43 16111 BROMMA
Telefon	+46(8) 80 21 60
E-post	kundservice@nitor.se

1.4 Telefonnummer för nödsituationer

I akuta fall: Ring 112, begär giftinformation.

AVSNITT 2: Farliga egenskaper

2.1 Klassificering av ämnet eller blandningen

Denna blandning är inte klassificerad som farlig vid bedömning enligt 1272/2008

2.2 Märkningsuppgifter

Faropiktogram	Ej tillämpligt
Signalord	Ej tillämpligt
Faroangivelse	Ej tillämpligt

2.3 Andra faror

Ej angivet.

AVSNITT 3: Sammansättning/information om beståndsdelar

3.2 Blandningar

Observera att tabellen visar kända faror för ingredienserna i ren form. Farorna minskas eller elimineras när de blandas eller späds ut, se Avsnitt 16d.

Beståndsdel	Klassificering	Koncentration
KROM(III)OXID		
CAS nr: 1308-38-9 EG nr: 215-160-9		>98 %
KROM(IV)OXID		
CAS nr: 12018-01-8 EG nr: 234-630-4	Eye Irrit. 2; H319	<0,01 %

Förklaringar till ingrediensernas klassificering och märkning ges i Avsnitt 16e. Officiella förkortningar är skrivna med normal stil. Med kursiv stil anges specifikationer och/eller kompletteringar som använts vid beräkning av blandningens klassifikation, se Avsnitt 16b.